

Supplementary information

Observation of the axion quasiparticle in 2D MnBi_2Te_4

In the format provided by the
authors and unedited

Supplemental Information for

This file includes:

- I. Additional data
 - I.1. Magnon data of 5SL MnBi₂Te₄
 - I.2. Additional magnon data of 6SL MnBi₂Te₄
 - I.3. Additional static Kerr data
 - I.4. Additional DAQ data of 6SL MnBi₂Te₄
 - I.5. Phonon data of 6SL MnBi₂Te₄
 - I.6. Other addition data and sanity check
- II. AFM Kerr and DAQ probed by DC *E* field
- III. Dark matter Axion detection
 - III.1. Detection sensitivity calculation
 - III.2. Future steps to build a functioning Axion detector
 - III.3. Comparison between the meV DAQ detector and two other proposed future detectors
- IV. Theoretical derivation for the layer Hall effect
- V. Tight binding model for MnBi₂Te₄
- VI. Additional discussion

I. Additional data

I.1. Magnon data for 5SL MnBi₂Te₄

In the main text, we focused on 6SL MnBi₂Te₄. For completeness, here we show the magnon data (and the effect of E -field) in 5SL MnBi₂Te₄. As shown in the TRMOKE data of 5SL MnBi₂Te₄ (Fig. S1), the out-of-phase magnon is the most prominent mode, consistent with previous results [1]. We then study the time-dependent magnetoelectric coupling α of 5SL MnBi₂Te₄. As shown in Fig. S2, both the DC and AC E field measurements do not show observable α oscillation.

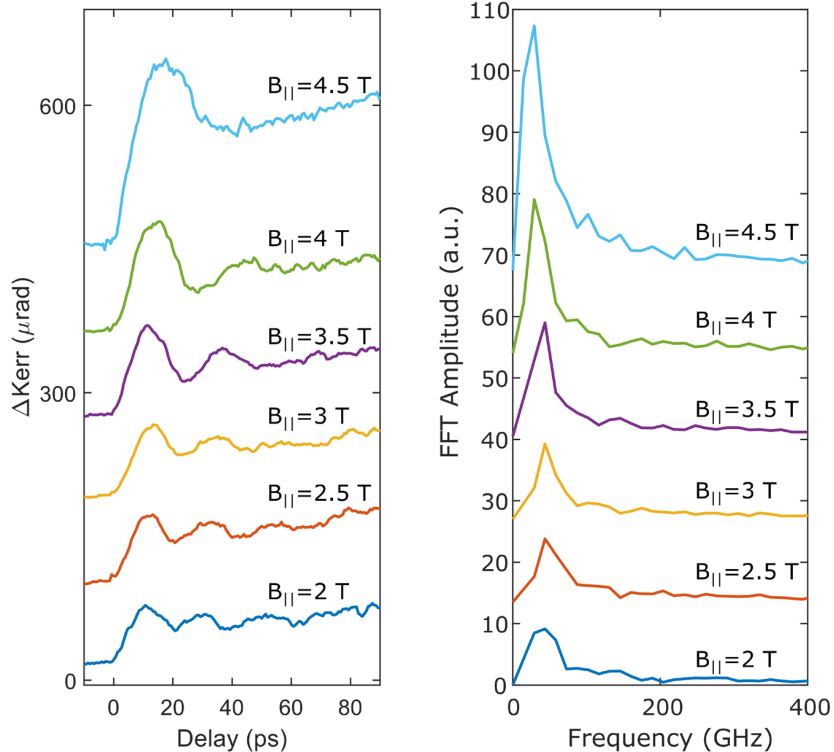


Figure S1: **a**, TRMOKE data and FFT analysis of 5SL MnBi₂Te₄ ($\lambda_{\text{pump}} = 1030$ nm, $\lambda_{\text{probe}} = 515$ nm)

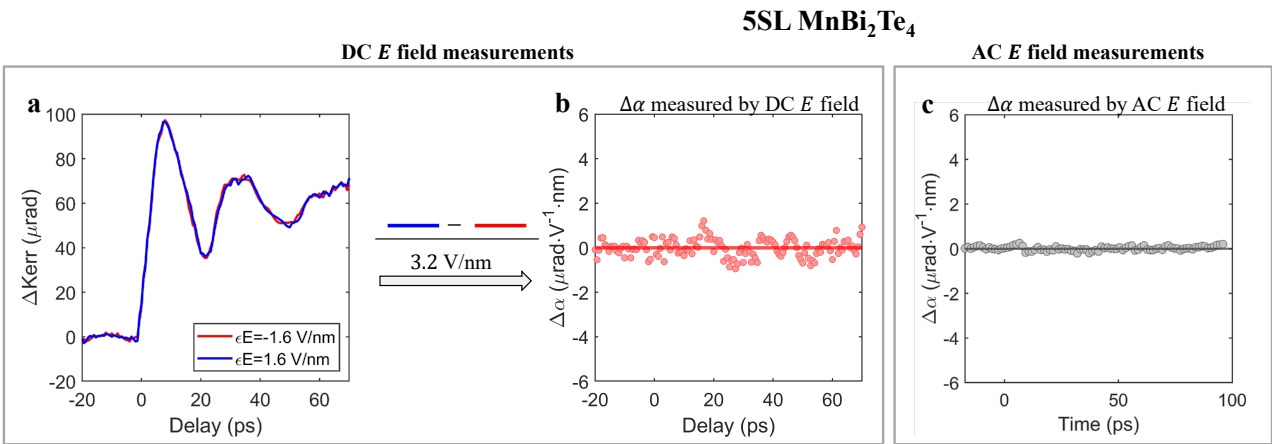


Figure S2: **E -field dependence of TRMOKE data of 5SL MnBi₂Te₄.** **a**, TRMOKE data at different DC E field values ($B_{||} = 3.5$ T). **b**, Time-resolved $\Delta\alpha$ is obtained by the difference of the TRMOKE data at ± 1.6 V/nm divided by 3.2 V/nm. **c**, Time-resolved $\Delta\alpha$ measured by AC E field dependent measurements.

I.2. Additional magnon data of 6SL MnBi₂Te₄

I.2.1 Theoretical calculation of magnon in 6SL MnBi₂Te₄

Using the standard Heisenberg model, we theoretically calculated the magnon modes in 6SL MnBi₂Te₄. Theoretically, we obtained six magnon modes, which can be classified based on the C_2 symmetry (Fig. S3). Specifically, we found that two out of the six magnon modes (+1A/-1A) resemble the in-phase and out-of-phase modes in bilayer or in the bulk limit. By further comparing our calculation with our experimental data (Fig. S4), we found that these two modes are likely to be the two experimentally observed magnon modes. Figure S5 studies how the equilibrium spin angles affect the Berry curvature oscillation. In Figs. S5a,b, the spin equilibrium angle was set to the same ($\pm 19.7^\circ$) across all layers. In Figs. S5c,d should be different for different layers. The spin equilibrium angles are calculated based on the Heisenberg model. We set the angles of the top and bottom layers to be the same ($\pm 19.7^\circ$). In particular, the angles of inner layers are larger because the inner layers feel stronger exchange coupling. The corresponding Berry curvature oscillation are similar to the previous, except for a small global shift (Fig. S5).

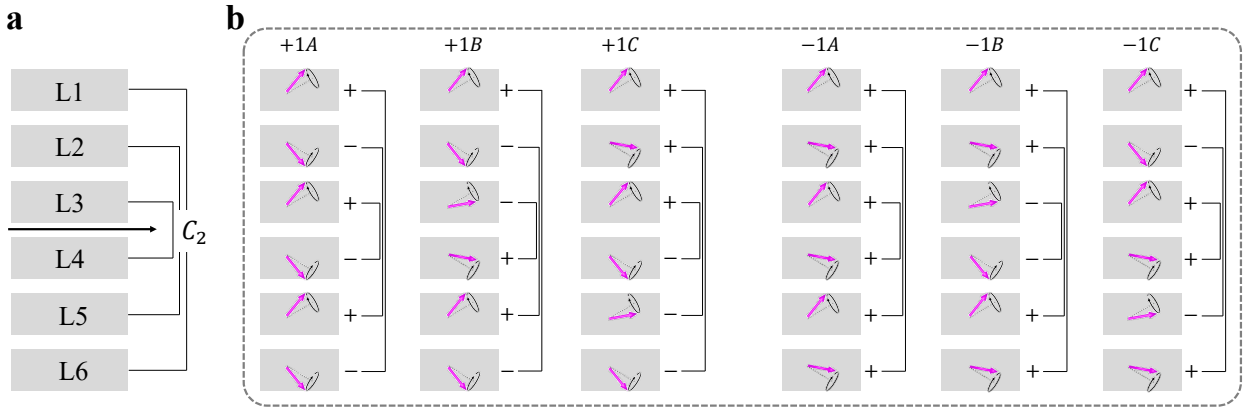


Figure S3: **a**, C_2 pairs in 6SL MnBi₂Te₄. **b**, Schematic illustration of the six magnon modes. The initial phase of the spin is denoted by the pink vector as well as the $+$, $-$ on the right-hand side of the layer. In this figure, the equilibrium angle is assumed to be the same for all layers for simplicity.

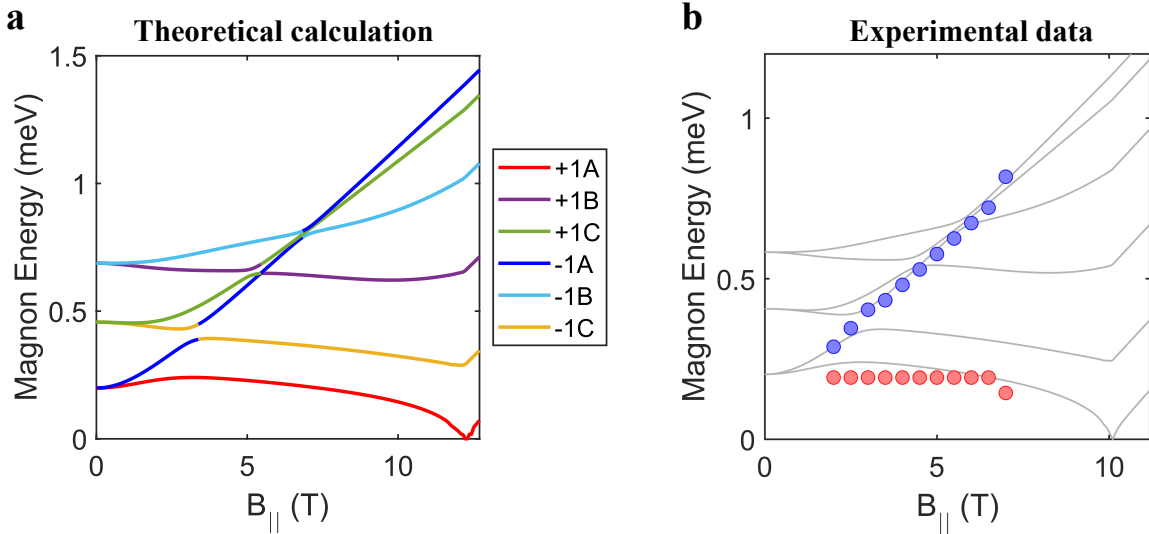


Figure S4: **a**, Calculated magnon energy as a function of $B_{||}$ for 6SL MnBi₂Te₄. The red and blue highlights the +1A and -1A modes. **b**, Red and Blue circles denote our experimentally measured energy of the out-of-phase and in-phase magnons. The black lines are the theoretical calculations same as panel (a). $J = 0.2954$ meV and $\kappa = 0.03130$ meV.

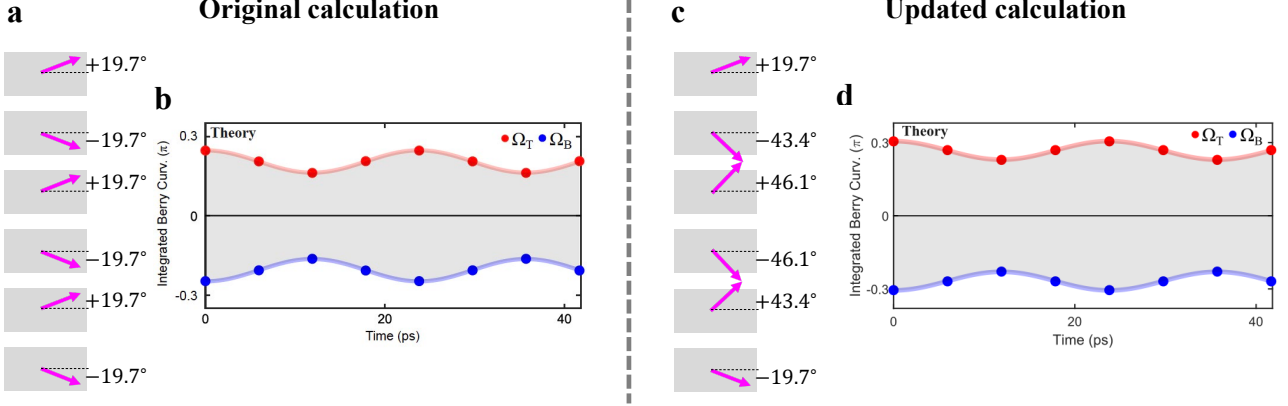


Figure S5: **a**, Calculation of Berry curvature oscillation of 6SL MnBi_2Te_4 . **b**, The spin equilibrium angles are assumed to be uniform ($\pm 19.7^\circ$) across all layers. The spin precession angle is 5° . **c**, The spin equilibrium angles are calculated based on the Heisenberg model. We set the angles of the top and bottom layers to be the same ($\pm 19.7^\circ$). The angles of inner layers are larger because the inner layers feel stronger exchange coupling. **d**, Corresponding Berry curvature oscillation.

I.2.2 Additional magnon data of WSe₂/6SL MnBi₂Te₄

Fig. S6 presents the pump photon energy and pump polarization dependence of magnon data in WSe₂/6SL MnBi₂Te₄. The magnon data does not depend on the pump polarization or pump photon energy, which suggests that the excitation mechanism is laser-heating induced coherent precession [2].

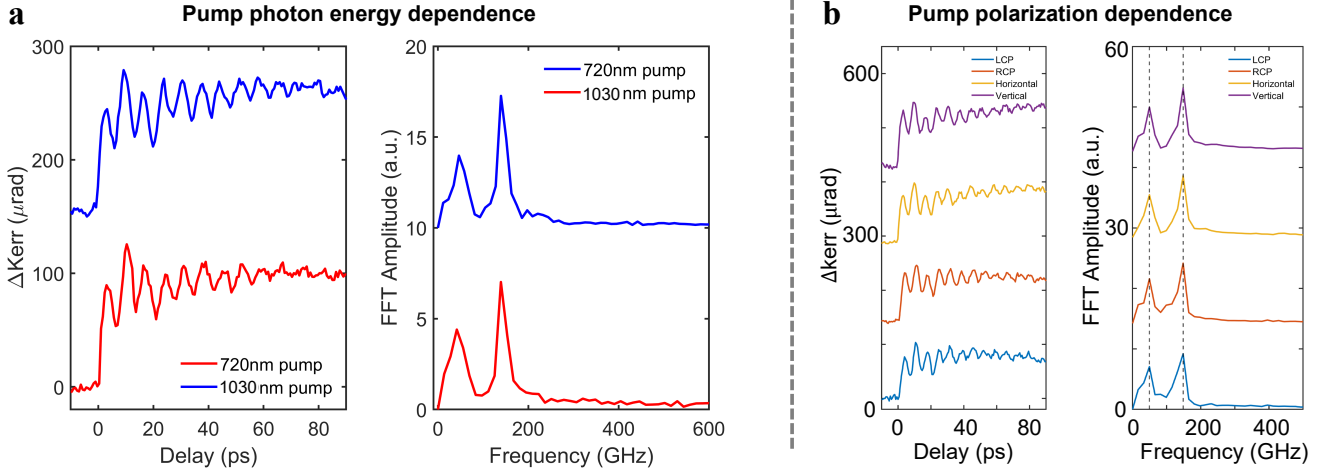


Figure S6: **a**, TRMOKE of WSe₂/6SL MnBi₂Te₄ using pump photon energies of 720 nm and 1000 nm. **b**, TRMOKE of WSe₂/6SL MnBi₂Te₄ using different pump polarizations.

I.3. Additional static Kerr data

Firstly, Fig. S7 shows the static Kerr vs B_{\perp} data in a 6SL MnBi₂Te₄ dual-gated device, which is consistent with [3], therefore confirming that the sample remains even-layered structure after microfabrications. Additional electric field dependence further demonstrates the magnetoelectric effect.

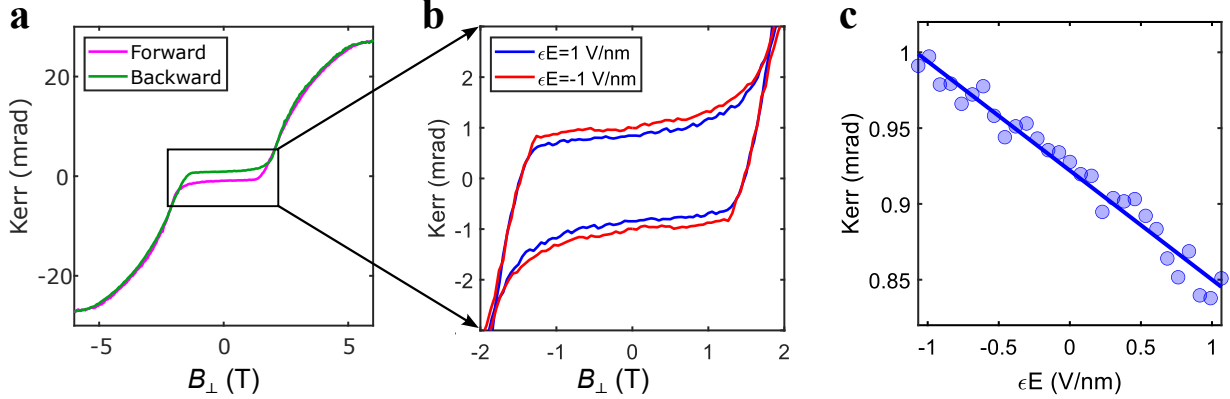


Figure S7: **a**, Static MOKE data of 6SL MnBi₂Te₄ as a function of out-of-plane B_{\perp} field. **b**, Zoomed-in view of the antiferromagnetic state at two different electric field E values. The amplitude of the MOKE changes by E field due to the magnetoelectric coupling. **c**, MOKE as a function of DC E field at $B_{\perp} = 0$. The linear E dependence of the MOKE amplitude shows the magnetoelectric coupling. $\lambda_{\text{probe}} = 515 \text{ nm}$.

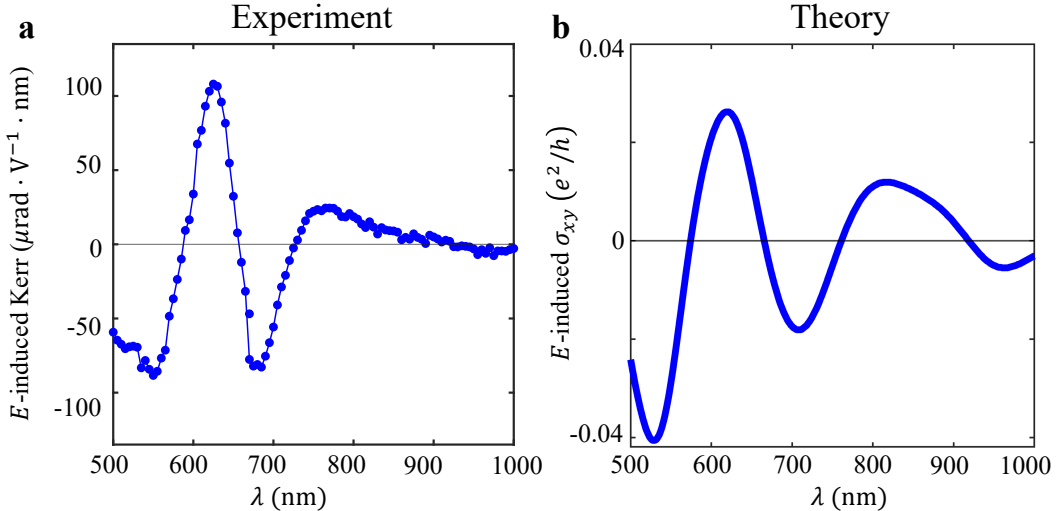


Figure S8: **a**, Experimentally measured E -field induced Kerr at different wavelengths. **b**, Theoretically calculated E -field induced σ_{xy} at different wavelengths.

Secondly, In addition the optical detection of magneto-electric coupling is based on the assumption that Kerr rotation measures magnetization.

- As shown in Fig. S9, we can measure the magnetization M_z of bulk MnBi₂Te₄ as a function of B_z using SQUID and compare with the Kerr vs. B_z of 6SL MnBi₂Te₄. Both the Kerr and M_z show a linear dependence on B_z , therefore suggesting that Kerr is proportional to magnetization in our system (Kerr $\propto B \propto M_z$).
- Fig. S8a shows the probe wavelength dependence of the E -field induced Kerr rotation. Furthermore, we theoretically calculated the E -field induced σ_{xy} , which shows a good agreement between data and calculation, based on Kerr $\propto \sigma_{xy}(\lambda) \propto \gamma(\lambda)M_z$. This result therefore suggests our conclusion that the

measured E -field induced Kerr rotation in 6SL MnBi₂Te₄ indeed reflects the E -field induced magnetization.

3. To further strengthen point 2 above, in our DFT calculation, we could calculate the E -induced σ_{xy} and E -induced M_z . As shown in Fig. S10, both σ_{xy} and M_z are linearly dependent on E . Hence, we could obtain Kerr $\propto \sigma_{xy} \propto E \propto M$, which demonstrates the proportionality between Kerr rotation and M_z .
4. We further measured the doping n dependence of the $\frac{\Delta \text{Kerr}}{\Delta E}$ (similar to the Fig. 4b of main text) using three wavelengths. If $\frac{\Delta \text{Kerr}}{\Delta E}$ vs. n is a good measure of $\alpha(n)$, then different wavelengths should give consistent results. Indeed, our data (Fig. S11) show similar behavior. We further elaborate on the logic: Because Kerr $\propto \gamma M_z$, its variation as a function of n , $\Delta \text{Kerr}/\Delta n$, may come from $\Delta M_z/\Delta n$ or $\Delta \gamma/\Delta n$. If it comes from M_z , the n dependence should be the same function at various wavelengths upon normalization. By contrast, if it comes from γ , then n dependence of γ should be different functions at various wavelengths. Furthermore, our measured $\frac{\Delta \text{Kerr}}{\Delta E}$ vs. n shows good agreement with the theoretically calculated $\alpha(n)$. Therefore, collectively, these evidences suggest that the measured n dependence mostly arises from changes in M_z .
5. Furthermore, we can achieve a symmetry-based, direct proof that our E -induced Kerr is measuring E -induced magnetization. As shown in Ref. [3], magnetization M_z induces both Kerr (reflection) and Faraday (transmission) rotation. By contrast, the AFM order L_z only shows up in Kerr but is absent in Faraday. Therefore, if the E -field induced signal shows up in both reflection (Kerr) and in transmission (Faraday), then it measures M_z . Figure S12 shows the simultaneous Kerr and Faraday measurements at different DC E field. we see that the linear-to- E effect exists in both reflection and transmission. But in reflection, there is a nonzero offset at $E = 0$ due to the AFM Kerr; In transmission, the Faraday rotation is zero at $E = 0$. Therefore, our simultaneous reflection and transmission measurements directly prove that the observed linear-to- E Kerr rotation is due to magnetization M_z .

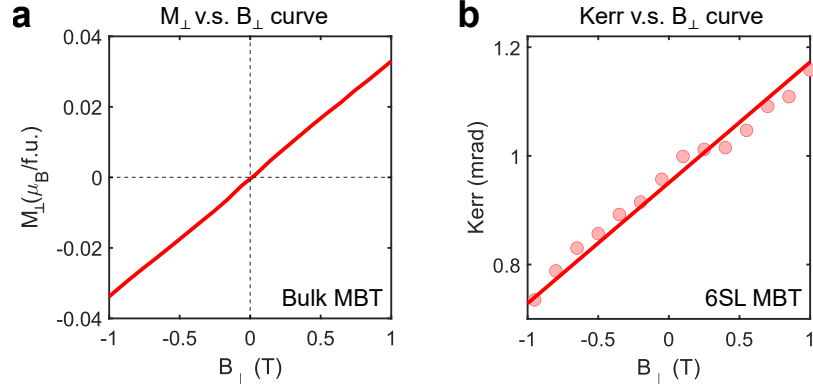


Figure S9: **a**, M_z - B_z of bulk MnBi₂Te₄ measured by SQUID. **b**, Kerr- B_z of 6SL MnBi₂Te₄.

Thirdly, static magnetic properties such as T_N and the spin flop field B_{spinflop} can also serve as an experimental check if J and K were strongly modified by gating (J : exchange coupling, K : anisotropy). As shown in Fig. S13, T_N and B_{spinflop} do not show observable dependence on n and E , suggesting that J and K are roughly invariant within the experimentally studied n and E range.

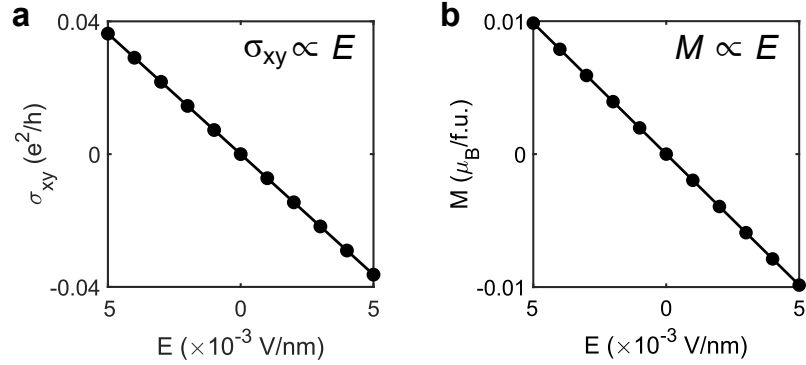


Figure S10: **a**, Theoretical calculation of σ_{xy} - E of 6SL MnBi₂Te₄. The wavelength of σ_{xy} is 515 nm. **b**, Theoretical calculation of M_z - E_z of 6SL MnBi₂Te₄.

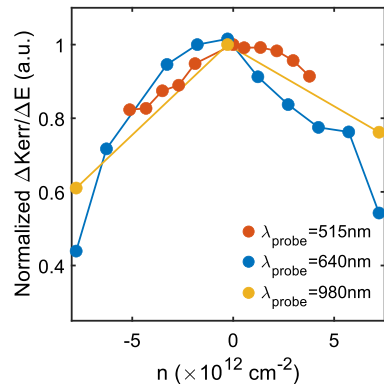


Figure S11: $\frac{\Delta\text{Kerr}}{\Delta E}$ vs. n measurement using three wavelengths (normalized at $n = 0$).

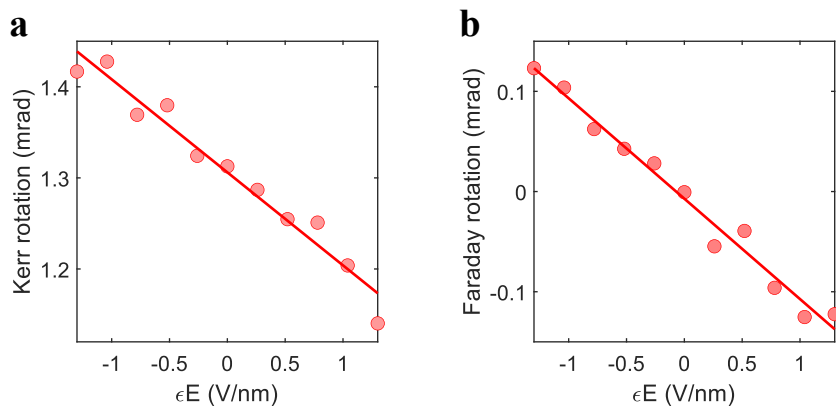


Figure S12: Simultaneous Kerr (**a**) and Faraday rotation (**b**) measurements as a function of E field for 6SL MnBi₂Te₄.

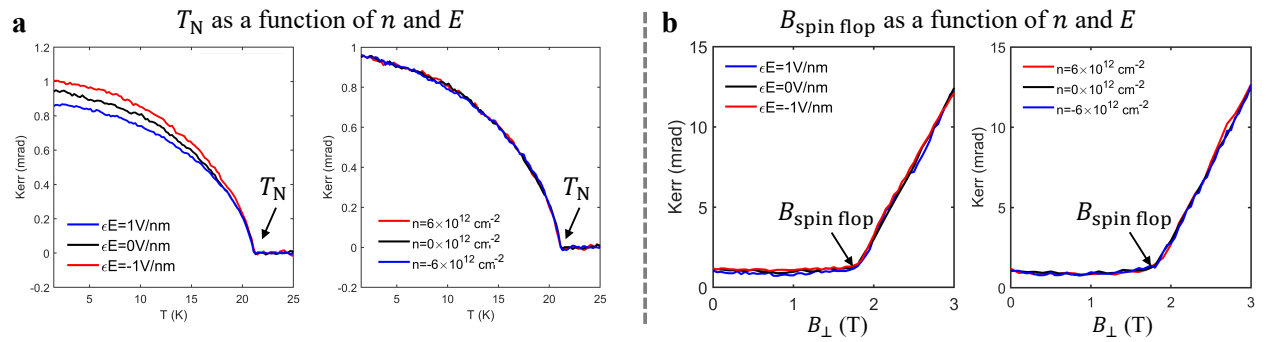


Figure S13: Static Kerr measurements of T_N (a) and $B_{\text{spin flop}}$ (b) as a function of n and E ($\lambda_{\text{probe}}=515$ nm).

I.4. Additional DAQ data of 6SL MnBi₂Te₄

I.4.1. Addressing competing mechanisms

We present additional data, to address competing mechanisms. In particular, if the electrostatic gating strongly modifies the exchange coupling J and magnetic anisotropy K , it might also change the TRMOKE signal. Thus, we investigated the n and E dependence of the TRMOKE signals. In particular, in even-layer MnBi₂Te₄, there are in total eight distinct dependences. I.e., how does the *frequency* (or **TRMOKE amplitude**) of the *in-phase* (or *out-of-phase*) magnon depend on n (or E). We found that the only observed change is that the TRMOKE amplitude shows a linear E dependence at the out-of-phase magnon frequency. If the exchange coupling J and the anisotropy K were strongly modified by gating, then we would expect both the frequency and TRMOKE amplitude of both magnon modes to show gate dependence (both n and E). Therefore, our results strongly suggest that the alternative effect that J and K are strongly modified is unlikely to be origin. Rather, the DAQ is a more plausible and consistent interpretation. Below, we present the corresponding data.

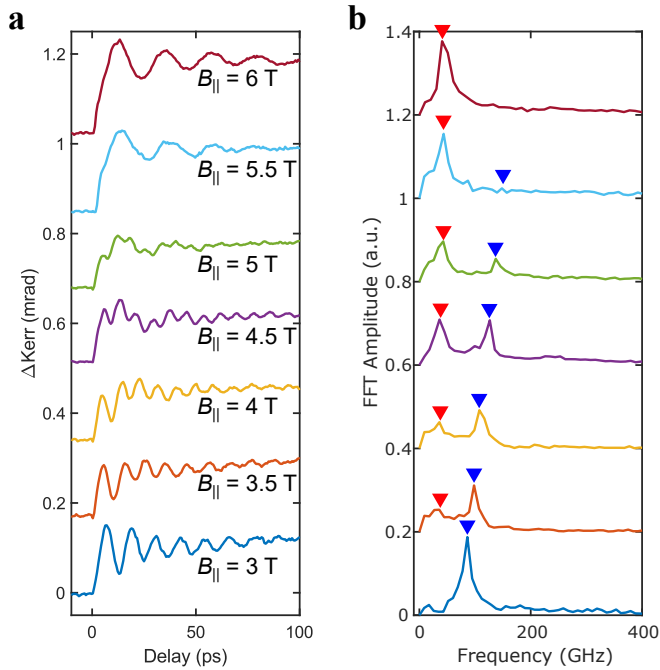


Figure S14: TRMOKE data of 6SL MnBi₂Te₄ at different B_{\parallel} field (red and blue triangles represent out-of-phase and in-phase magnons).

Figure S14 shows the TRMOKE data of 6SL MnBi₂Te₄. The signal consists of both the AFM Kerr and the regular Kerr, therefore can detect both the in-phase and out-of-phase magnons. As shown in Fig. S14, **the in-phase magnon is prominent at small B_{\parallel} , whereas the out-of-phase magnon becomes strong at large B_{\parallel} .**

We set $B_{\parallel} = 3 \text{ T}$, where the in-phase magnon is prominent. As shown in Fig. S15, the in-phase magnon shows no observable n and E dependence in terms of both the frequency and TRMOKE amplitude.

We set $B_{\parallel} = 6 \text{ T}$, where the out-of-phase magnon is prominent. As shown in Fig. S16, the out-of-phase magnon shows no observable n dependence in terms of both the frequency and TRMOKE amplitude as well as no observable E dependence in terms of the frequency. The only observed change is that the TRMOKE amplitude shows a linear E dependence at the out-of-phase magnon frequency.

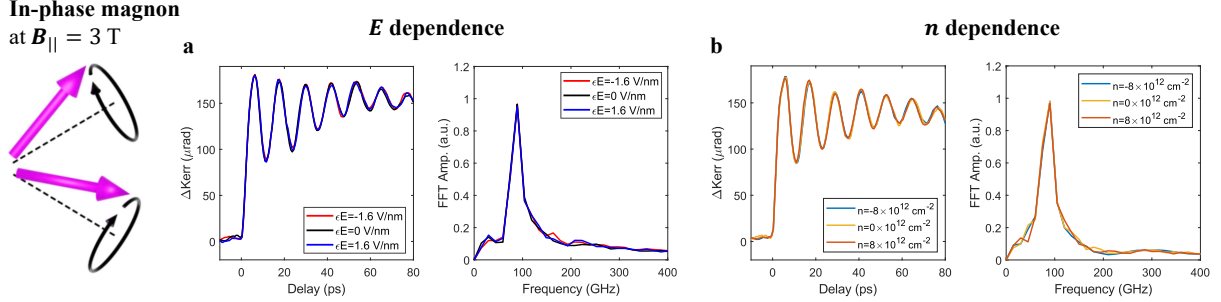


Figure S15: Gate dependent TRMOKE data at $B_{\parallel} = 3$ T. The in-phase magnon shows no observable n and E dependence in terms of both the frequency and TRMOKE amplitude. $\lambda_{\text{pump}} = 1030$ nm, $\lambda_{\text{probe}} = 515$ nm.

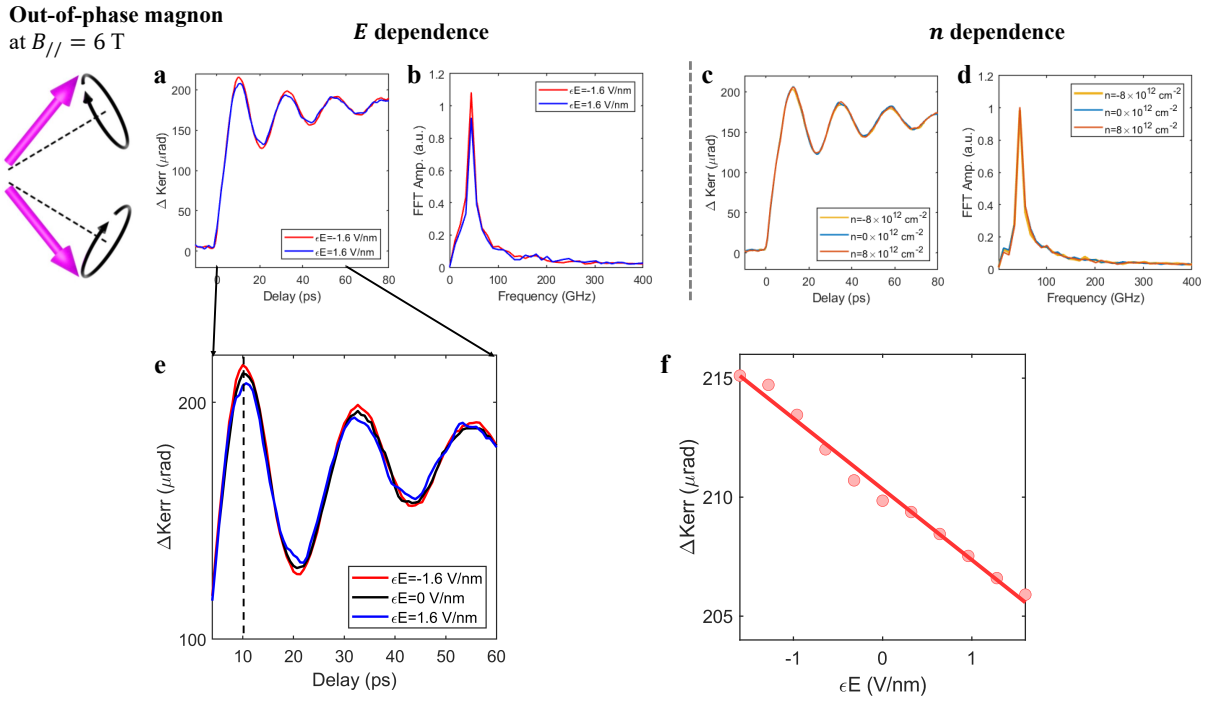


Figure S16: Gate dependent TRMOKE data at $B_{\parallel} = 6$ T. Top row: The out-of-phase magnon shows no observable n and E dependence in terms of both the frequency and TRMOKE amplitude. Bottom row: A zoomed-in view of the TRMOKE with three different E values. E dependence TRMOKE at delay time 10 ps (dotted line on the left). $\lambda_{\text{pump}} = 1030$ nm, $\lambda_{\text{probe}} = 515$ nm.

I.4.2. E and n dependence of TRMOKE measured by DC and AC methods

We now try to obtain the time-resolved α by DC E field method, and show that the result is fully consistent with the AC E field modulation method adapted in the main text. Specifically, we first park the magnetic field at $B_{\parallel} = 6$ T, where the out-of-phase magnon is prominent. Figure S17a shows the TRMOKE at different DC E values (same data as Fig. S16). In order to obtain the time-resolved $\Delta\alpha$, we subtract the TRMOKE data at $E = \pm 1.6$ V/nm and divide it by 3.2 V/nm. The result, shown in Fig. S17b, shows an oscillation of α . Therefore, we can detect the α oscillation (the DAQ) by DC E field method; The result (Fig. S17b) is consistent with that of AC E field lock-in method shown in Fig. S17c (the AC data has better signal to noise ratio).

Moreover, we can also the magnetic field at $B_{\parallel} = 4.5$ T, where both the in-phase and out-of-phase magnons are excited. When we perform E -field dependence (both DC and AC), we can also see the α

oscillation at the out-of-phase magnon frequency with fully consistent results (Fig. S18).

Furthermore, we performed similar comparison between DC and AC doping n dependence. Figure S19 shows the TRMOKE data at $\pm n$ values (same data as Fig. S16). The TRMOKE does not show significant change with n . As such, their difference (Fig. S19b) is nearly zero. Consistent result is obtained if one AC modulates the doping n (Fig. S19c).

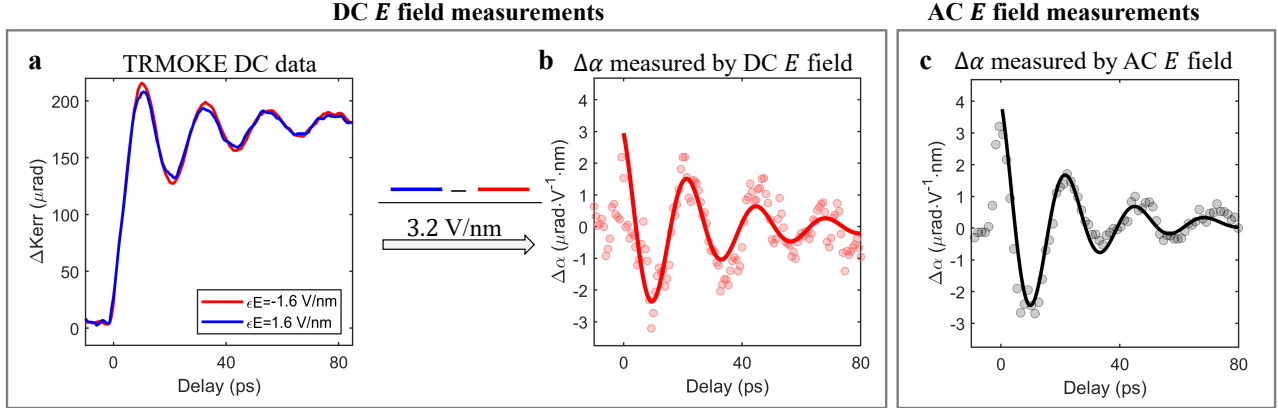


Figure S17: Comparison between DC and AC E field dependent measurements at 6 T. a, TRMOKE data at different DC E field values (same data as Fig. S16). b, Time-resolved $\Delta\alpha$ is obtained by the difference of the TRMOKE data at ± 1.6 V/nm divided by 3.2 V/nm. c, Time-resolved $\Delta\alpha$ measured by AC E field-dependent measurements.

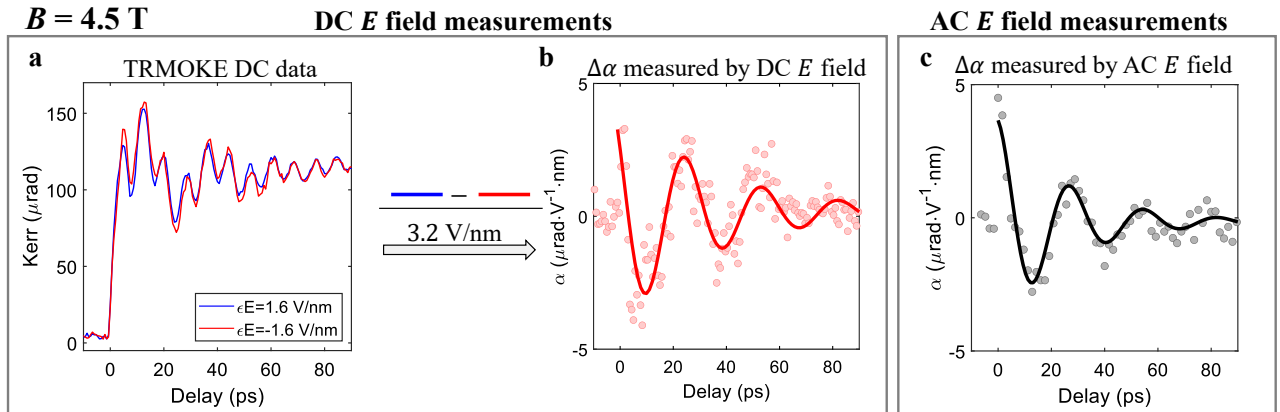


Figure S18: Comparison between DC and AC E field dependent measurements at 4.5 T. a, TRMOKE data at different DC E field values at 4.5 T, both in-phase and out-of-phase magnons are clearly observed. b, Time-resolved $\Delta\alpha$ is obtained by the difference of the TRMOKE data at ± 1.6 V/nm divided by 3.2 V/nm. c, Time-resolved $\Delta\alpha$ measured by AC E field-dependent measurements.

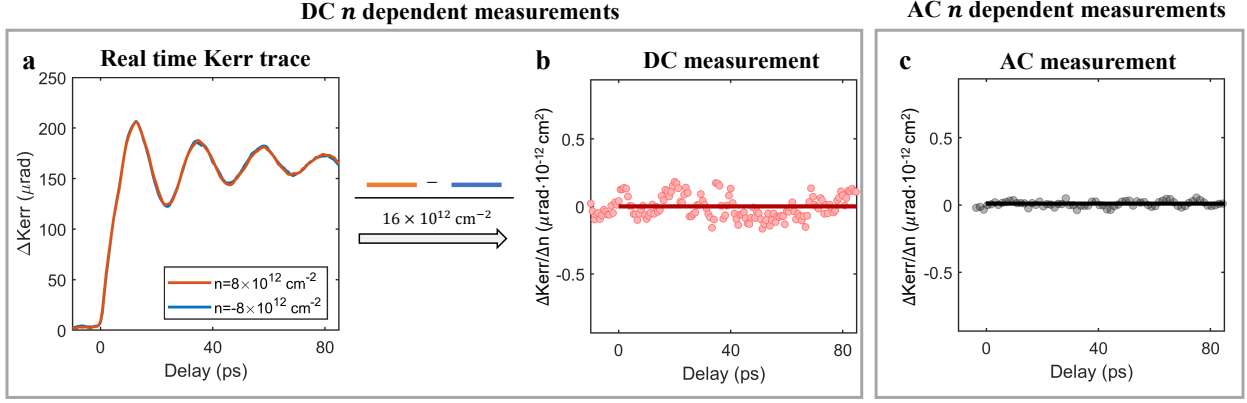


Figure S19: Comparison between DC and AC doping n dependent measurements. **a**, TRMOKE data at different DC n values. **b**, The difference of the TRMOKE data at $\pm 8 \times 10^{12} \text{ cm}^{-2} \cdot \text{V/nm}$ divided by $16 \times 10^{12} \text{ cm}^{-2} \cdot \text{V/nm}$. **c**, AC doping n dependent measurements of the TRMOKE.

I.4.3. Doping dependence of DAQ data

In the main text, all $\Delta\alpha$ measurements were performed with the Fermi level at charge neutrality ($n = 0$). Here, we present the n dependence of $\Delta\alpha$ measurements for completeness. As shown in Fig. S20, the $\Delta\alpha$ oscillation frequency remains the same at different n values, but the oscillation amplitude decreases as one changes from charge neutrality ($n = 0$) to both electron-doped and hole-doped regimes. This observation is consistent with our static α versus n measurements shown in Fig. 4b of the main text.

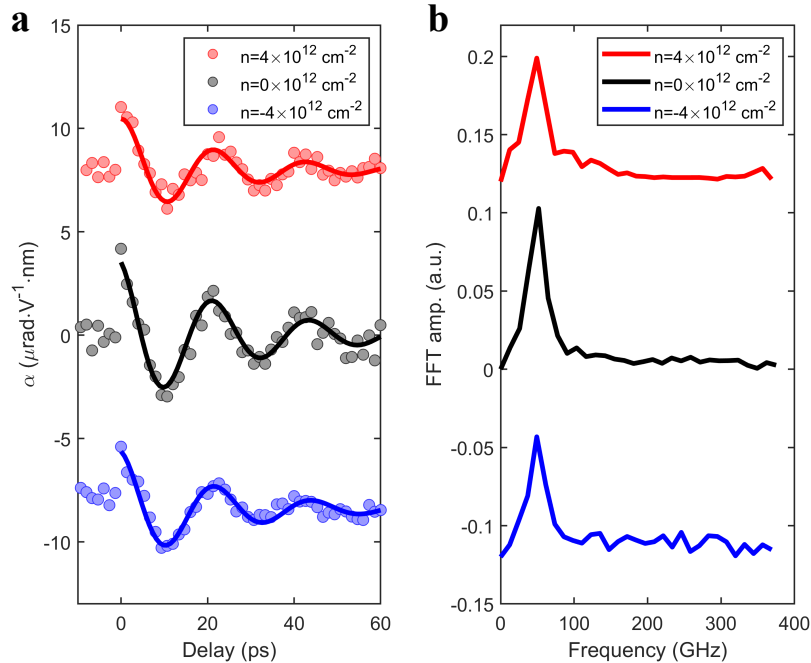


Figure S20: Time-resolved α data at different n values ($B_{||}=6$ T).

I.4.4. Reproducibility of DAQ

We present the reproducibility of DAQ at different locations on the sample (Fig. S21).

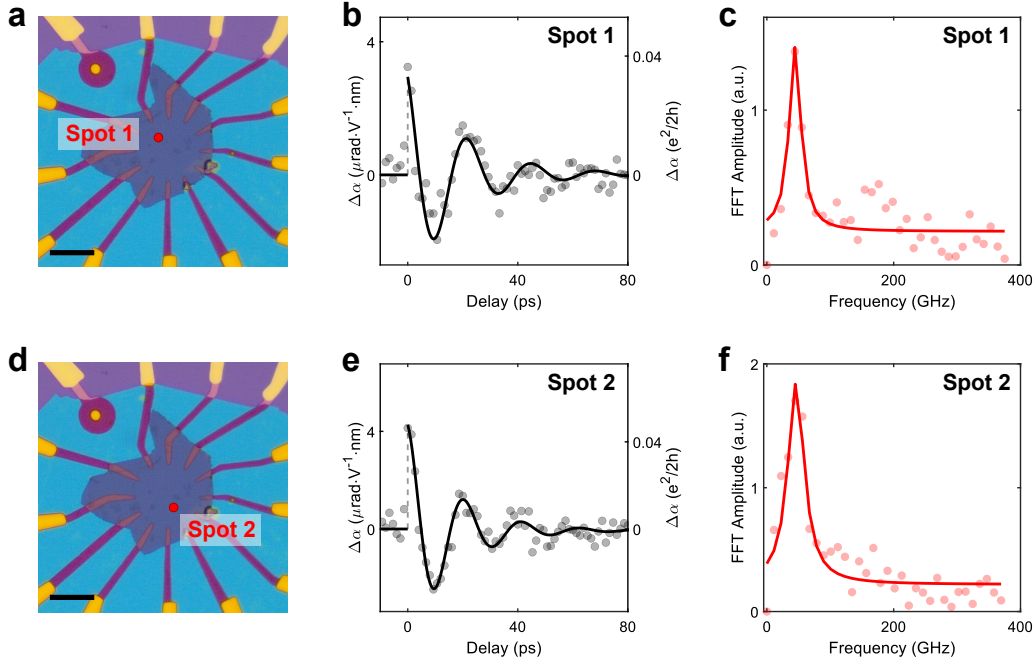


Figure S21: **Reproducibility of dynamical Axion quasiparticle at different locations.** **a-c** At laser spot-1 location, time-dependent α measurements and FFT. **d-f**, Same as **a-c** for a different location on the sample. Scale bar: $20 \mu\text{m}$

I.4.5. Direct comparison of DAQ and magnon

Here, we show the direct comparison of DAQ (measured by $\Delta\alpha$) and magnons (measured by TRMOKE) in Fig. S22. Regarding both the $B_{||}$ and T dependence, the DAQ agrees very well with the out-of-phase magnon.

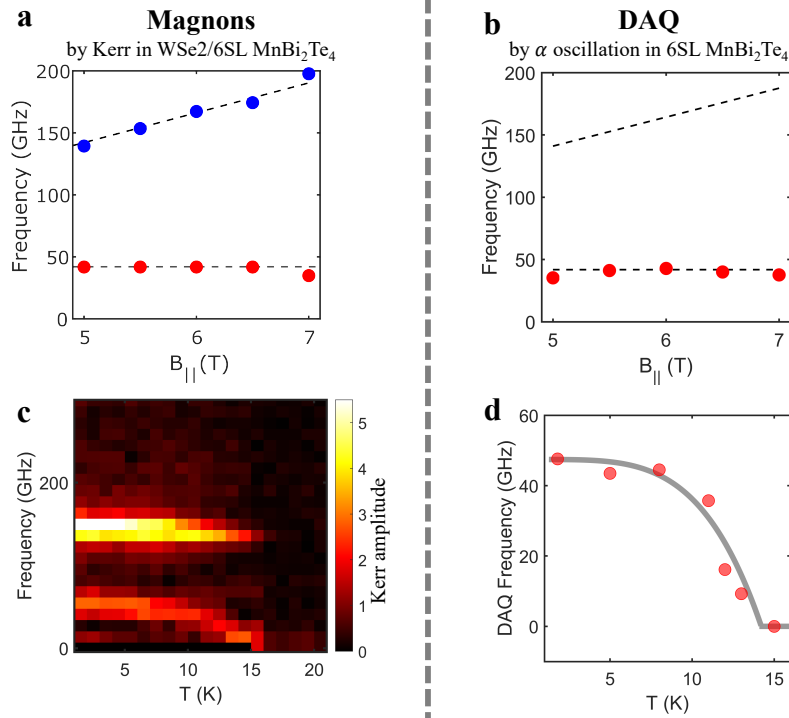


Figure S22: **Comparison between magnon and DAQ** **a**, Magnon frequency probed by the TRMOKE in WSe₂/6SL MnBi₂Te₄ heterostructure. **b**, The DAQ by the α oscillation in 6SL MnBi₂Te₄. **c-d** Temperature dependence of magnon and DAQ, respectively.

I.5. Phonon data of 6SL MnBi₂Te₄

In the main text, we focused on the magnon-induced effect. We discuss phonon induced effect in this section. Theoretically, we use DFT to compute the phonon frequencies at Γ point of 6SL MnBi₂Te₄. As shown in Fig. S23, the lowest phonon frequency is ~ 160 GHz, which is much higher than the experimentally observed DAQ frequency. Experimentally, we can observe the breathing phonon at ~ 200 GHz by time-resolved reflectivity ($\Delta R/R$) measurements, which is also consistent with [4]. In addition, we also investigated the gate dependence of this phonon mode. As shown in Fig. S24, our data show no observable gate dependence and no observable temperature dependence across T_N .

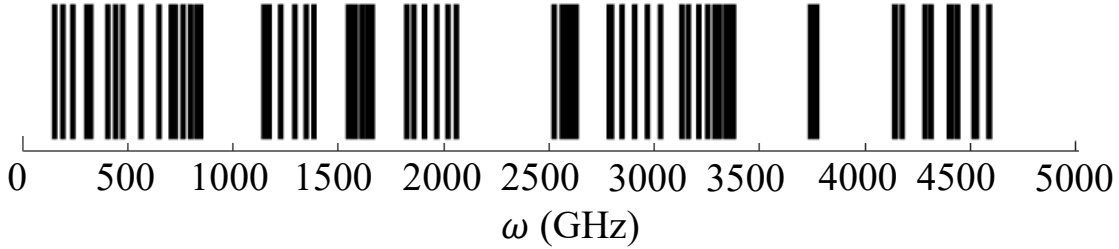


Figure S23: **Theoretically calculated phonon frequency**

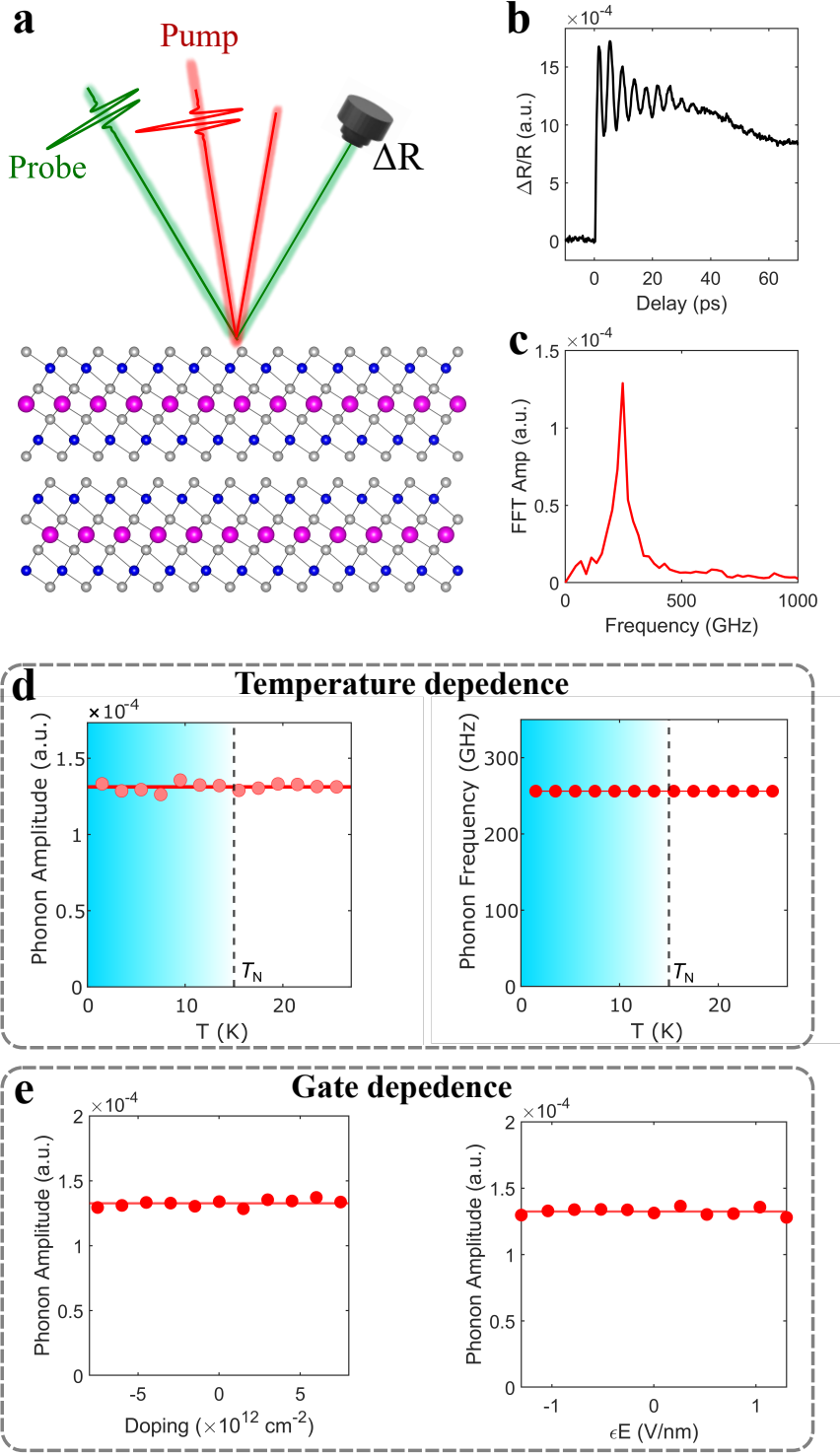


Figure S24: **a-c**, Time-resolved reflectivity data showing the breathing phonon oscillation. **d-f**, Temperature and gate dependence of the phonon amplitude (measured by the Fourier peak value). $\lambda_{\text{pump}} = 1030 \text{ nm}$, $\lambda_{\text{probe}} = 515 \text{ nm}$,

I.6. Other addition data and sanity check

In this section, we present other additional data to support our conclusion in the main text. As shown in Fig. S25, we have performed additional experiments including the $M_{\parallel} - H_{\parallel}$ measurements on bulk MnBi₂Te₄, the optical linear dichroism ($\propto M_{\parallel}^2$) in 6SL MnBi₂Te₄ and the magnetoelectric coupling ($\alpha \propto L_z$) in 6SL MnBi₂Te₄. These experiments confirmed the expected magnetic ground state under a finite in-plane magnetic field B_{\parallel} . In addition, we present the optical images of all devices used in our experiments in Fig. S26. Furthermore, Fig. S27 and Fig. S28 showed the reproducibility and symmetry analysis of the magneto-electric effect.

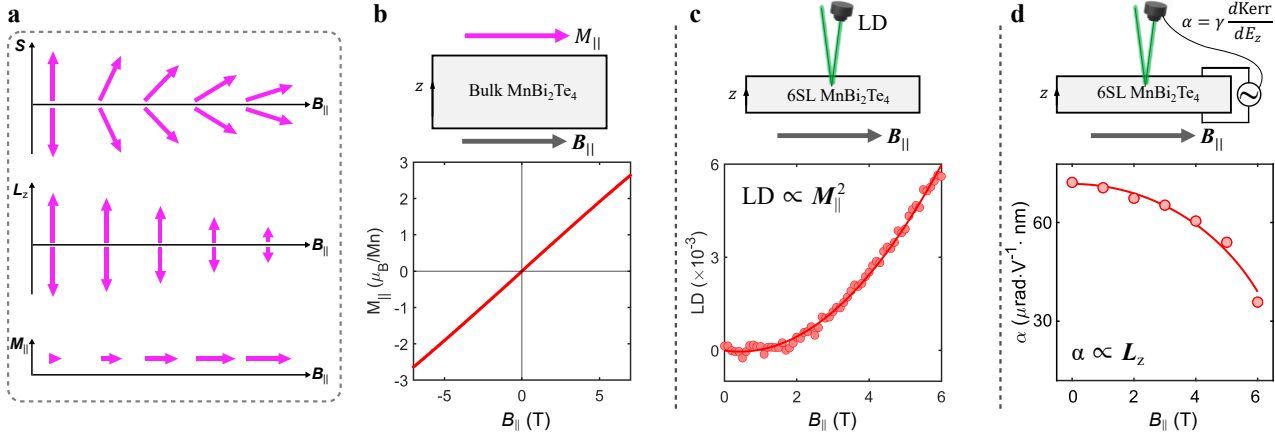


Figure S25: **a**, Schematic illustration of how the Mn spins cant with increasing B_{\parallel} and the evolution of L_z and M_{\parallel} . **b**, $M_{\parallel} - B_{\parallel}$ data in bulk MnBi₂Te₄. **c**, Optical linear dichroism (LD) as a function of B_{\parallel} in 6SL MnBi₂Te₄. **d**, α (measured by E -field induced Kerr rotation) as a function of B_{\parallel} in 6SL MnBi₂Te₄.

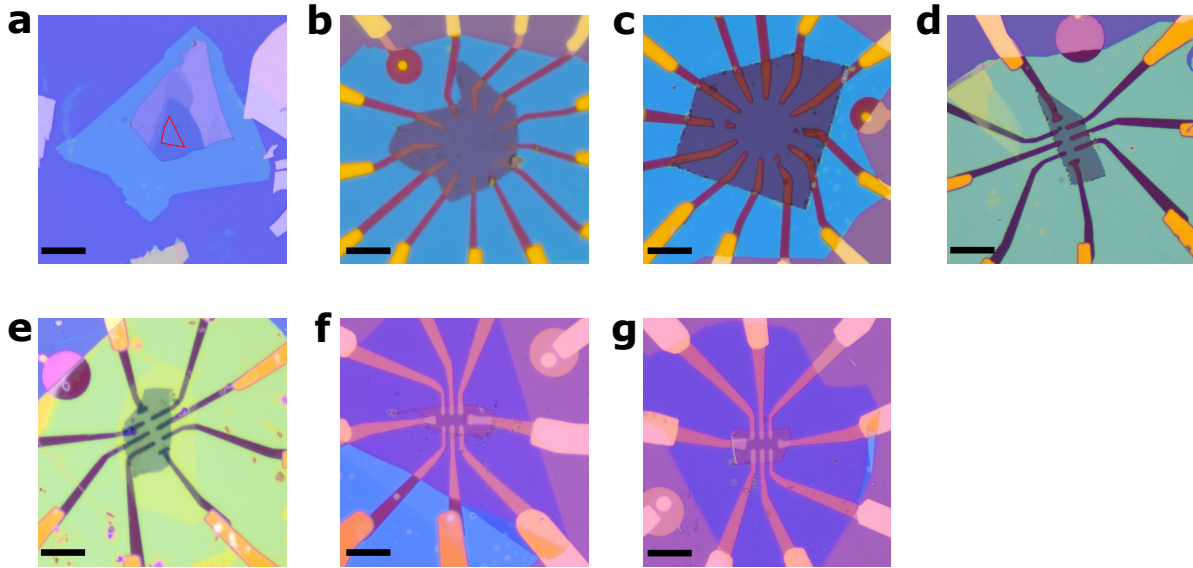


Figure S26: **Optical microscope device images.** **a** Dev1 is a heterostructure of 6-SL MnBi₂Te₄ and monolayer WSe₂ (red triangle). **b-g** Device images of 6-SL MnBi₂Te₄ for Dev2-Dev7. Scale bar: 20 μm

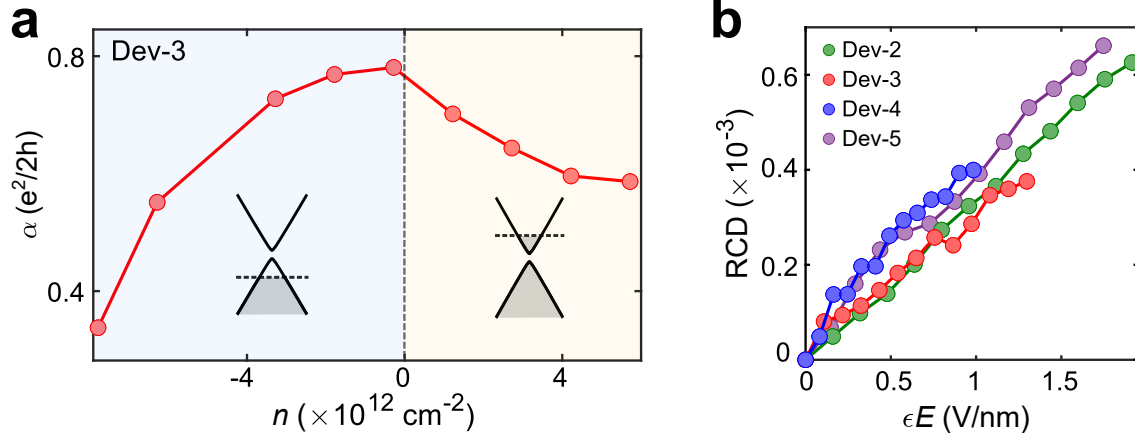


Figure S27: **Reproducibility data for static magnetoelectric coupling α measurements.** Probe wavelength is at 600 nm. We note that Kerr and RCD gives similar results.

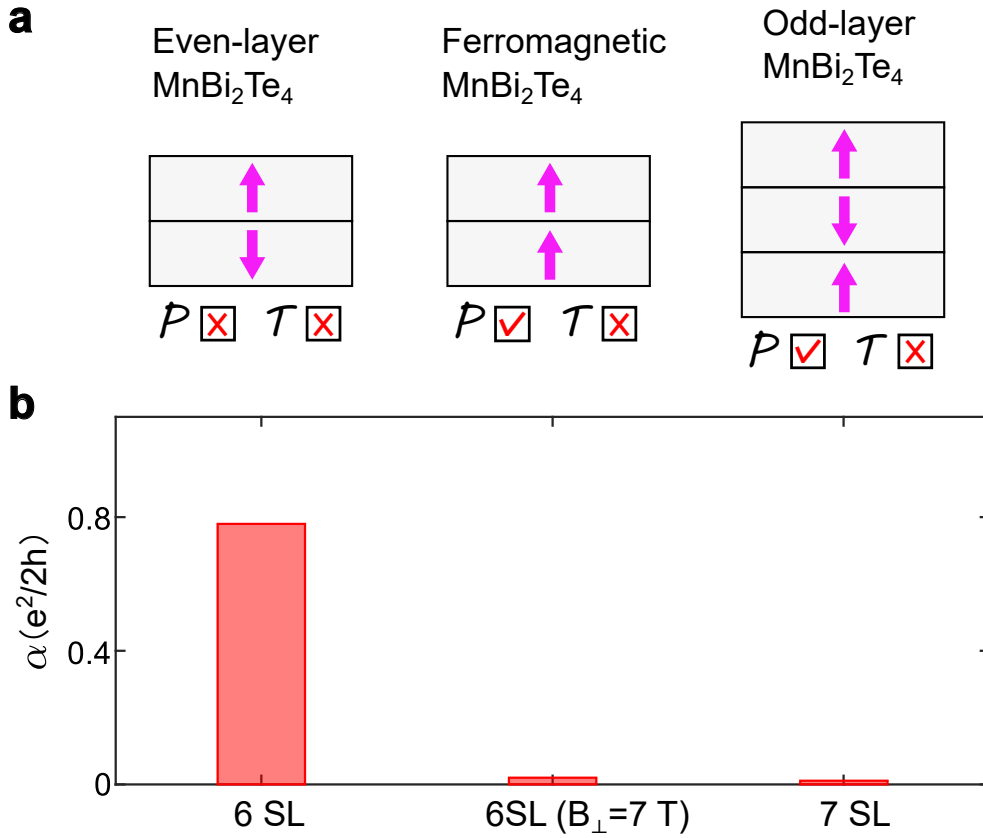


Figure S28: **Symmetry analysis for static magnetoelectric coupling α measurements.** **a**, The magnetoelectric coupling α requires the breaking of both time-reversal \mathcal{T} and space-inversion \mathcal{P} symmetries. Even-layer antiferromagnetic MnBi_2Te_4 breaks both \mathcal{P} and \mathcal{T} , therefore is expected to show a nonzero α . By contrast, ferromagnetic MnBi_2Te_4 and odd-layer antiferromagnetic MnBi_2Te_4 both respect \mathcal{P} , therefore are expected to show zero α . **b**, Measured magnetoelectric coupling for 6SL antiferromagnetic MnBi_2Te_4 , ferromagnetic 6SL MnBi_2Te_4 ($B_\perp = 7 \text{ T}$) and 7SL antiferromagnetic MnBi_2Te_4 .

II The AFM Kerr effect and DAQ probed with DC E -field

II.1. The AFM Kerr effect

The regular Kerr effect is proportional to magnetization M_z . However, in a PT -symmetric antiferromagnet with zero magnetization (breaking P and T but preserves PT) such as Cr_2O_3 [5] or even-layer MnBi_2Te_4 [3], there is an AFM Kerr effect, which is proportional to the AFM order L_z . Moreover, the PT -symmetric AFM order L_z leads to the AFM Kerr effect but no Faraday effect. By contrast, M_z leads to both nonzero Kerr and Faraday effect. These conclusions have been experimentally demonstrated in MnBi_2Te_4 by Ref. [3].

- 6SL MnBi_2Te_4 is a PT -symmetric AFM with zero net magnetization. It shows the AFM Kerr effect. Moreover, it shows zero Faraday effect (Fig. S29).
- 5SL MnBi_2Te_4 has an uncompensated magnetization (M_z), which is like a ferromagnet. So it supports both nonzero Kerr effect and Faraday effect, both proportional to M_z (Fig. S29).

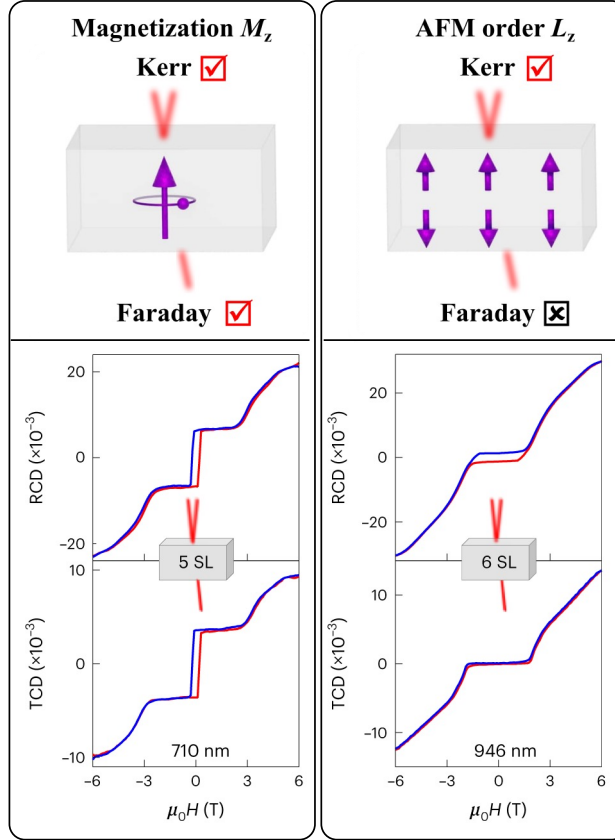


Figure S29: The net magnetization M_z can be probed by both Kerr and Faraday. The AFM order L_z can only be probed by Kerr. These conclusions have been experimentally demonstrated by Ref. [3]. Here we reproduce the Fig. 3 of Ref. [3]. We note that Kerr/Faraday have the same symmetry as RCD/TCD (reflection circular dichroism and transmission circular dichroism).

II.2. The AFM Kerr rotation shows up as a DC offset at $E=0$

Therefore, for 6SL MnBi_2Te_4 , if we apply a DC E field, we expect that the AFM Kerr ($\propto L_z$) already shows up at $E=0$ (i.e., a nonzero offset); on top of that, there will also be a regular Kerr ($\propto M_z$) that is linearly proportional to E field due to the magnetoelectric coupling α . Indeed, this can be seen from our data under DC E field (Fig. S30). By contrast, if we apply AC E field modulation, then the lock-in signal would only detect the Kerr rotation that is linear to E (Fig. S30), therefore allowing us to isolate the magnetoelectric coupling signal.

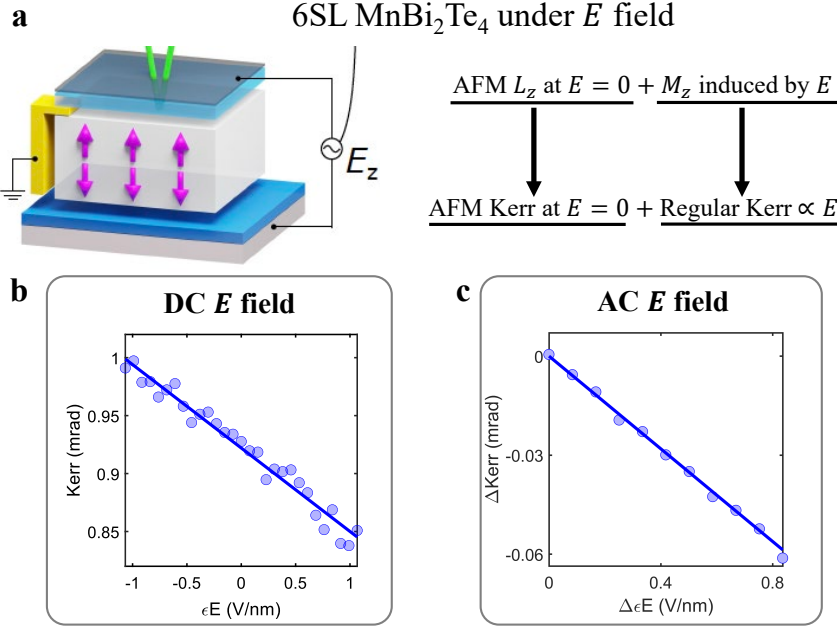


Figure S30: **a**, Analysis of the different order parameters (L_z and M_z) of 6SL MnBi₂Te₄ under E field. **b**, Kerr data as a function of DC E field. **c**, Kerr data as a function of AC E field modulation.

II.3. The AFM Kerr does not have any linear-in- E contribution

One important question is whether the AFM Kerr can also support a linear-in- E component. Here, we show that, based on the symmetry analysis, the AFM Kerr can NOT have any linear-in- E contribution. The symmetry analysis is as follows: The AFM Kerr has distinct symmetry properties; it breaks P and T but respects PT . As a result, let us suppose the AFM Kerr has a linear-in- E component: AFM Kerr = χE . We can perform PT operation to both sides of the equation. Under PT , AFM Kerr is invariant, but E becomes $-E$. Therefore $\chi = 0$. In other words, the AFM Kerr effect cannot have any linear-in- E component (it can only have even powers of E including E^0). In the next subsection, we further prove that the observed linear-in- E Kerr purely comes from the E -induced magnetization, i.e., the magnetoelectric coupling.

II.4. The observed linear-in- E MOKE arises from E -induced magnetization

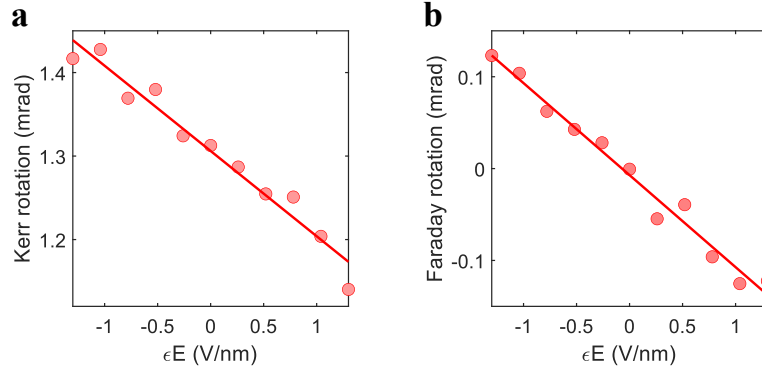


Figure S31: Simultaneous Kerr (**a**) and Faraday rotation (**b**) measurements as a function of DC E field for 6SL MnBi₂Te₄. Both Kerr and Faraday show an linear-in- E effect due to the E -induced M_z . The Kerr signal has an additional offset at $E = 0$ due to the AFM Kerr effect.

We now aim to prove that the observed linear-in- E Kerr comes from the E -induced magnetization. As we discussed above, M_z will induce both Faraday and Kerr rotation, but L_z will only induce Kerr rotation.

Therefore, by testing if there is also an E -induced signal in Faraday effect, we can know if the E -induced Kerr signal is AFM Kerr ($\propto L_z$) or regular Kerr ($\propto M_z$). We have performed new measurements to study Kerr and Faraday simultaneously using DC E field method. As shown in Fig. S31, our data clearly shows that the linear-in- E signal exists in both Kerr and Faraday. Therefore, our simultaneous reflection and transmission measurements directly prove that the observed linear-in- E Kerr rotation is the regular Kerr $\propto M_z$.

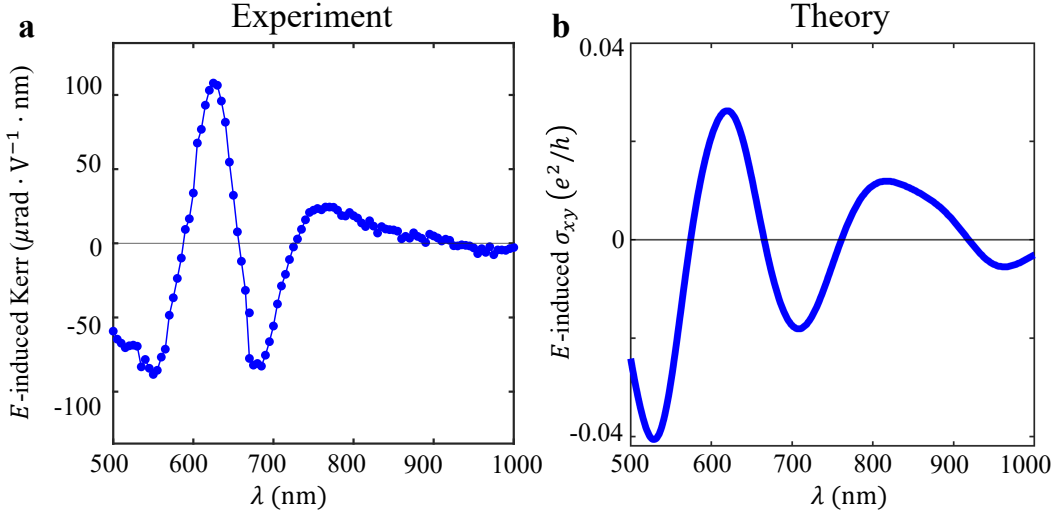


Figure S32: **a**, Experimentally measured E -field induced Kerr at different wavelengths. **b**, Theoretically calculated E -field induced σ_{xy} at different wavelengths.

To further prove that the observed E -induced Kerr comes from magnetization. We note that formally, the regular Kerr rotation measures the off-diagonal (Hall) part of the optical conductivity σ_{xy} , which has identical symmetry properties as the out-of-plane magnetization M_z . Therefore, we can write $\text{Kerr}(\lambda) \propto \sigma_{xy}(\lambda) \propto \gamma(\lambda)M_z$. In order to verify this, we have (1) experimentally measured the E -field induced Kerr rotation as a function of the wavelength λ and (2) theoretically calculated the wavelength dependence of the E -field $\sigma_{xy}(\lambda)$. As shown in Fig. S32, we see a good agreement between data and calculation, which therefore strengthens our conclusion that the measured the E -field induced Kerr rotation in 6SL MnBi₂Te₄ indeed reflects the E -field induced magnetization (i.e., the magnetoelectric coupling α).

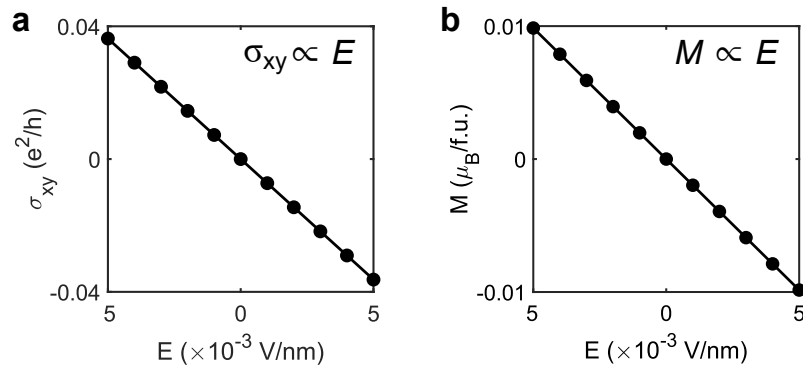


Figure S33: **a**, Theoretical calculation of the optical σ_{xy} - E of 6SL MnBi₂Te₄. The wavelength of σ_{xy} is 515 nm. **b**, Theoretical calculation of M_z - E_z of 6SL MnBi₂Te₄.

We can further strengthen the logic of the above proof as follows: First, the good agreement of the wavelength dependence demonstrates that our measured E -induced Kerr comes from E -field $\sigma_{xy}(\lambda)$. This proof is quite solid because it is not based on a single number (e.g. at one wavelength); Rather it is based on the agreement of an entire curve (e.g. many wavelengths). Second, in our DFT calculation, we obtained the E -induced $\sigma_{xy}(\lambda)$ by calculating $\sigma_{xy}(\lambda)$ at different E values. We can also calculate the net magnetization

M_z at those E values. Fundamentally, we first compute a band structure of 6SL MnBi₂Te₄ for every E value, then the corresponding $\sigma_{xy}(\lambda)$ and M_z can be calculated based on the calculated band structure, see expressions below. As shown in Fig. S33, both σ_{xy} and M_z are linearly dependent on E . Hence, we showed Kerr $\propto \sigma_{xy} \propto E \propto M_z$.

$$M_z^{\text{orb.}} = \frac{e}{\hbar d} \text{Im} \sum_n \int_{\varepsilon_{n\mathbf{k}} \leq \mu} \frac{dk_x dk_y}{(2\pi)^2} \langle \partial_{k_x} u_{n\mathbf{k}} | H_{\mathbf{k}} + \varepsilon_{n\mathbf{k}} - 2\mu | \partial_{k_y} u_{n\mathbf{k}} \rangle,$$

$$\sigma_{xy}(\omega) = \frac{e^2}{\hbar d} \int \frac{dk_x dk_y}{(2\pi)^2} \sum_{n,m} f_{mn\mathbf{k}} \frac{i(\varepsilon_{m\mathbf{k}} - \varepsilon_{n\mathbf{k}}) \langle u_{n\mathbf{k}} | i\partial_{k_x} | u_{m\mathbf{k}} \rangle \langle u_{m\mathbf{k}} | i\partial_{k_y} | u_{n\mathbf{k}} \rangle}{(\varepsilon_{m\mathbf{k}} - \varepsilon_{n\mathbf{k}}) - \hbar\omega - i\eta}. \quad (\text{S1})$$

II.5. TRMOKE of 6SL MnBi₂Te₄

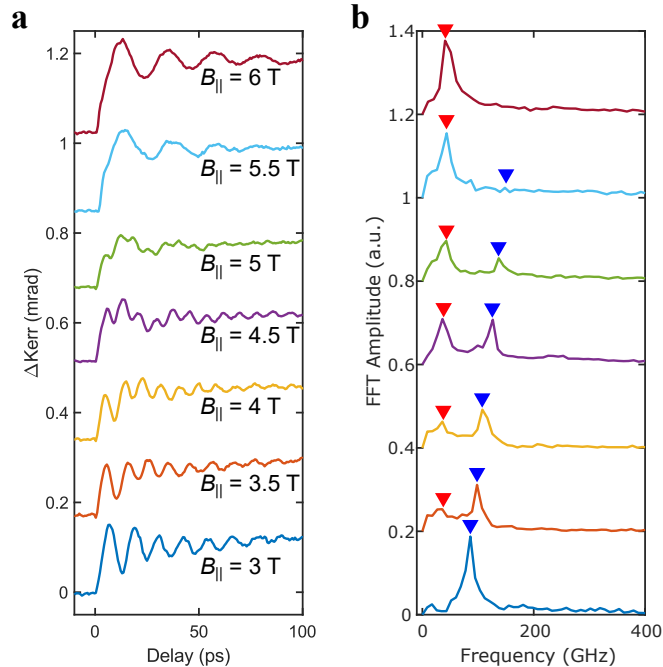


Figure S34: TRMOKE data of 6SL MnBi₂Te₄ (no WSe₂) at different B_{\parallel} field (red and blue triangles represent out-of-phase and in-phase magnons).

We now proceed to the time-resolved MOKE data. We have shown that the MOKE signal consists of two parts: the regular Kerr and the AFM Kerr.

- The regular Kerr is proportional to the net magnetization M_z . Hence, it can detect the in-phase magnon, because the in-phase magnon features an oscillating M_z .
- The AFM Kerr is proportional to the AFM order parameter L_z reported in [3]. Hence, it can detect the out-of-phase magnon, because the out-of-phase magnon features an oscillating L_z .

As shown in Fig. S34, both magnon modes are observed. **The in-phase magnon is prominently excited at small B_{\parallel} , whereas the out-of-phase magnon is prominently excited at large B_{\parallel} .**

II.6. TRMOKE at different DC E and n values

We set $B_{\parallel} = 3$ T, where the in-phase magnon is prominent. As shown in Fig. S35, the in-phase magnon shows no observable n and E dependence in terms of both the frequency and TRMOKE amplitude.

We set $B_{\parallel} = 6$ T, where the out-of-phase magnon is prominent. As shown in Fig. S36, the out-of-phase magnon shows no observable n dependence in terms of both the frequency and TRMOKE amplitude as well

as no observable E dependence in terms of the frequency. The only observable effect is that the TRMOKE amplitude shows a linear in E dependence at the out-of-phase magnon frequency, which is exactly the α oscillation. These systematic data also provide an important cross-check in terms of what is observable/not observable: 7 out of 8 dependences show no effect NOT due to insufficient resolution; Under the same conditions, we clearly observe linear E dependence of TRMOKE amplitude at the out-of-phase frequency.

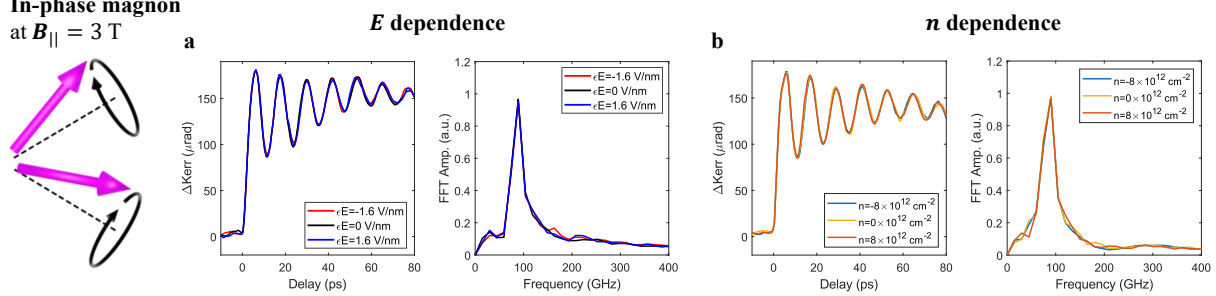


Figure S35: Gate dependent TRMOKE data at $B_{\parallel} = 3$ T. The in-phase magnon shows no observable n and E dependence in terms of both the frequency and TRMOKE amplitude. $\lambda_{\text{pump}} = 1030$ nm, $\lambda_{\text{probe}} = 515$ nm.

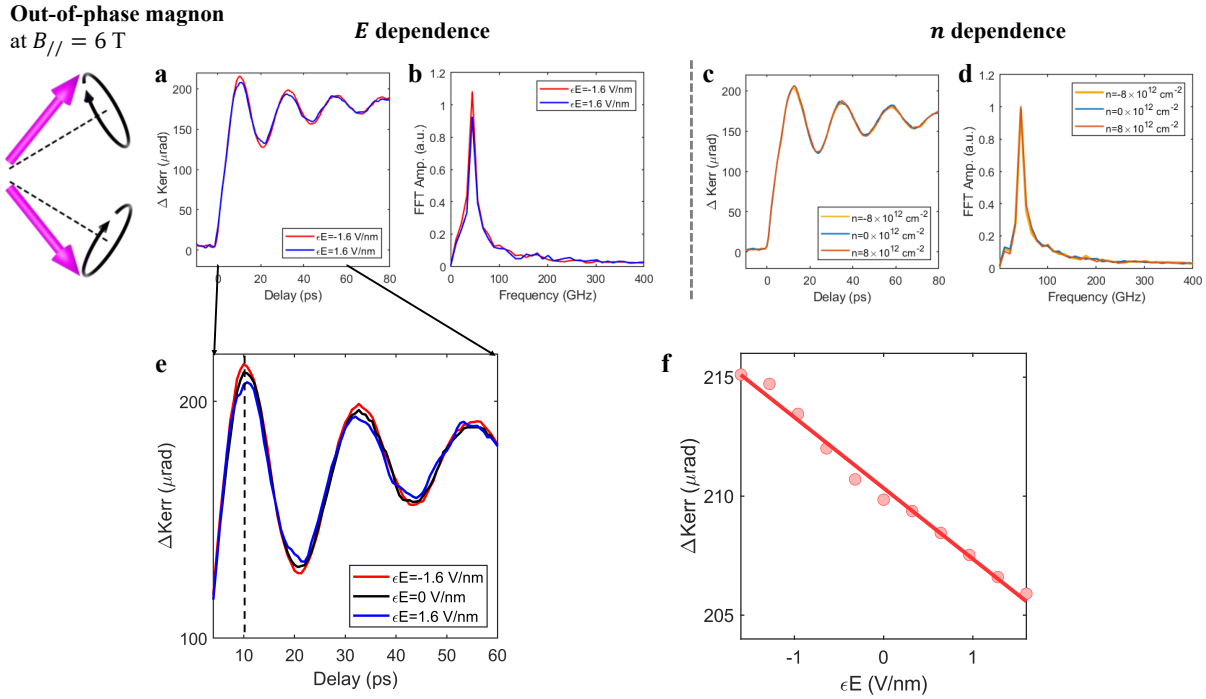


Figure S36: Gate dependent TRMOKE data at $B_{\parallel} = 6$ T. Top row: The out-of-phase magnon shows no observable n and E dependence in terms of both the frequency and TRMOKE amplitude. Bottom row: A zoomed-in view of the TRMOKE with three different E values. E dependence TRMOKE at delay time 10 ps (dotted line on the left). $\lambda_{\text{pump}} = 1030$ nm, $\lambda_{\text{probe}} = 515$ nm.

Fig. S37 presents a summary of the above results. In 6SL MnBi₂Te₄, we have systematically studied in total eight distinct dependences. I.e., how does the frequency (or TRMOKE amplitude) of the in-phase (or out-of-phase) magnon depend on n (or E). Seven out of eight dependences show no observable effect. The only exception is that the TRMOKE amplitude shows a linear-in- E dependence at the out-of-phase magnon frequency, which is the α oscillation. Moreover, we further show in SI.I (see Figs. S1 and S2) that there is no gate dependence for the TRMOKE of 5SL layer MnBi₂Te₄. If the exchange coupling J and the anisotropy κ

were strongly modified by gating, then we would expect both the frequency and TRMOKE amplitude of both magnon modes to show gate dependence (the n dependence is typically even stronger than E dependence, according to previous studies in $\text{Cr}_2\text{Ge}_2\text{Te}_6$ [6] and CrI_3 [7]). Also, we would expect similar effect in both even and odd layers. By contrast, if J and κ are roughly unchanged but the results were due to the DAQ (the α oscillation), then we would only expect a linear-in- E TRMOKE signal at the out-of-phase magnon frequency in even layer. Therefore, our results strongly suggest that the alternative effect that J and κ are strongly modified is unlikely to be origin. Rather, the DAQ is a more plausible and consistent interpretation.

	OUT-OF-PHASE MAGNON		IN-PHASE MAGNON	
	Frequency	TRMOKE amplitude	Frequency	TRMOKE amplitude
n	No change	No change	No change	No change
E	No change	Linear E dep.	No change	No change

Figure S37: A summary of the gate dependence of the magnon frequency and TRMOKE amplitude in 6SL MnBi_2Te_4 .

II.7. DAQ probed DC E field

We now try to obtain the time-resolved α by DC E field method, and show that the result is fully consistent with the AC E field modulation method adapted in the main text. Specifically, we first park the magnetic field at $B_{\parallel} = 6$ T, where the out-of-phase magnon is prominent. Figure S38a shows the TRMOKE at different DC E values (same data as Fig. S36). In order to obtain the time-resolved $\Delta\alpha$, we subtract the TRMOKE data at $E = \pm 1.6$ V/nm and divide it by 3.2 V/nm. The result, shown in Fig. S38b, shows an oscillation of α . Therefore, we can detect the α oscillation (the DAQ) by DC E field method; The result (Fig. S38b) is consistent with that of AC E field lock-in method shown in Fig. S38c (the AC data has better signal to noise ratio).

Moreover, we can also set the magnetic field at $B_{\parallel} = 4.5$ T, where both the in-phase and out-of-phase magnons are excited. When we perform E -field dependence (both DC and AC), we can also see the α oscillation at the out-of-phase magnon frequency with fully consistent results (Fig. S39).

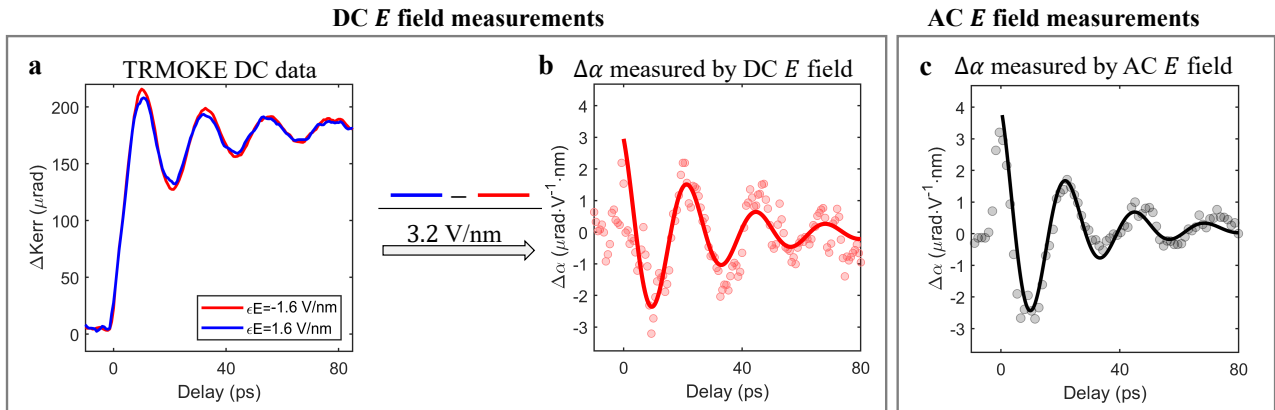


Figure S38: Comparison between DC and AC E field dependent measurements at 6 T. a, TRMOKE data at different DC E field values (same data as Fig. S36). b, Time-resolved $\Delta\alpha$ is obtained by the difference of the TRMOKE data at ± 1.6 V/nm divided by 3.2 V/nm. c, Time-resolved $\Delta\alpha$ measured by AC E field-dependent measurements.

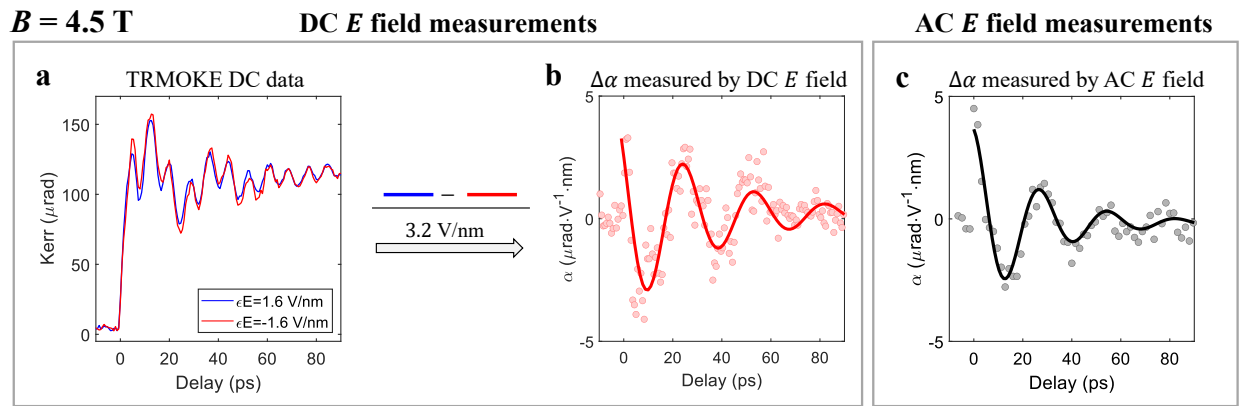


Figure S39: Comparison between DC and AC E field dependent measurements at 4.5 T. a, TRMOKE data at different DC E field values at 4.5 T, both in-phase and out-of-phase magnons are clearly observed. b, Time-resolved $\Delta\alpha$ is obtained by the difference of the TRMOKE data at ± 1.6 V/nm divided by 3.2 V/nm. c, Time-resolved $\Delta\alpha$ measured by AC E field-dependent measurements.

III. Dark Matter Axion Detection

III.1 Detection sensitivity calculation

Table 1 describes how we estimated the values of the parameters needed for the sensitivity calculation of the dark matter Axion detection using DAQ [8].

Parameter	Description	Reference Values	Comments
ρ_{DM}	Local Dark matter Axion density	0.4 GeV/cm ³	Estimation from astrophysics [9]
f_Θ	DAQ decay constant	82 eV	DFT calculations, see below
m_{DAQ}	DAQ mass	0.18 meV	Experimental data in this work
n	Dielectric constant	6.4	DFT calculation
Γ_m	Magnetic impurity density	0.7×10^{-3}	Value estimated from [10]
Γ_ρ	THz conductance	0.2×10^{-3}	DFT calculation
A	Detector Area	0.16 m ²	Large sample grown by MBE [11]
d	Sample thickness	0.4 mm	Optimal thickness based on [8]
B	External magnetic field	1-10 T	Typical cryostat conditions
η	Single photon detector efficiency	0.95	Estimated from [12]
λ_d	Dark count rate	10^{-5} Hz	Estimated based on [12]

Table 1: Parameter estimation values for dark matter Axion detector sensitivity calculation

f_Θ is given by $f_\Theta = g\sqrt{J}$ [8], Where J is the spin wave stiffness, and $g = \delta L/\delta\theta$ describes the strength of the DAQ (L is the antiferromagnetic order parameter). Extended Data Fig. 7 shows θ vs. L for 6SL MnBi₂Te₄, from which we get $g = 0.042$ eV. J is defined as follows based on [13]. We could write down the Hamiltonian for bulk MnBi₂Te₄:

$$\mathcal{H} = \sum_{i=1}^5 d_i \Gamma_i$$

$$\Gamma_{1,2,\dots,5} = (\tau_1 \sigma_3, -\tau_1 \sigma_2, \tau_1 \sigma_1, \tau_3 \sigma_0, \tau_0 \sigma_3)$$

$$d_{1,2,\dots,5} = \left(\frac{A_1}{c} \sin(k_z c), \frac{A_2}{a} \sin(k_x a), -\frac{A_2}{a} \cos(k_y a), M_0 + 2 \frac{M_1}{c^2} (1 - \cos(k_z c)) + 2 \frac{M_2}{a^2} [2 - \cos(k_z a) + \cos(k_y a)], (-1)^l m_5 \right)$$

, where l denotes the bulk MnBi₂Te₄ layer number, and a, c are lattice constants. The tight-binding model parameters are given by: $A_1 = 2.7023$ eV·Å, $A_2 = 3.1964$ eV·Å, $M_1 = 11.9048$ eV·Å², $M_2 = 9.4048$ eV·Å², $M_0 = -0.04$ eV, $m_5 = 0.03$ eV, $a = 4.334$ Å, $c = 40.91$ Å. With the tight-binding model above, the J of bulk MnBi₂Te₄ can be calculated as: $J = \int \frac{d^3 k}{(2\pi)^3} \frac{\sum_{i=1}^4 q_i^2}{16 \sum_{i=1}^5 q_i^2}$. As a result, we found $J = 3.612 \times 10^{-4}$ eV⁻³ Å⁻³. By taking the astrophysics convention of $\hbar = c = 1$, we could obtain $f_\Theta = g\sqrt{J} = 82$ eV.

The dielectric constant $\epsilon = \chi + 1$, where χ is the electric susceptibility. χ was calculated using,

$$\chi_{ij}(\omega) = \frac{e^2}{\hbar V} \sum_{n \in \text{occ}, m \in \text{unocc}, \mathbf{k}} \frac{2\omega_{mn}}{\omega_{mn}^2 - \omega^2} \text{Re}[r_{nm}^i r_{mn}^j] \quad (\text{S2})$$

Here, V is the system volume, $r_{mn}^i = \langle \psi_m | \hat{r}^i | \psi_n \rangle$ is the position matrix element, and $\hbar\omega_{mn} = \epsilon_m - \epsilon_n$ is the difference in energy eigenvalues for the Bloch state $|\psi_m\rangle$ and $|\psi_n\rangle$.

Resonant frequency: As shown in Ref. [8], the resonant frequency for Axion detection is given by

$$\omega_r = \omega_j = \sqrt{\omega_{\text{DAQ polariton}}^2 + \delta\omega_j^2} = \sqrt{\omega_{\text{DAQ}}^2 + C^2 B^2 + \delta\omega_j^2}$$

$$\text{, where } \delta\omega_j^2 = \frac{\Delta_j^2 b^2}{n^2 d^2 \omega_{\text{DAQ polariton}}^2}.$$

Here we show that $\delta\omega_j$ is indeed negligibly small, as shown in Fig. S40a. As such, the Axion-polariton frequency can be simplified as $\sqrt{\omega_{\text{DAQ}}^2 + C^2 B_{\parallel}^2}$. Based on our estimation, the value of C is around 0.615

$\text{meV}\cdot\text{T}^{-1}$. Figure S40b show how ω_{LO} is tuned by B_{\parallel} based on $C = 0.615 \text{ meV}\cdot\text{T}^{-1}$ (ω_{LO} is the dark matter detection mass). Our result shows that for a magnetic field less than 10 T, ω_{LO} can be tuned by B_{\parallel} to cover a large meV region.

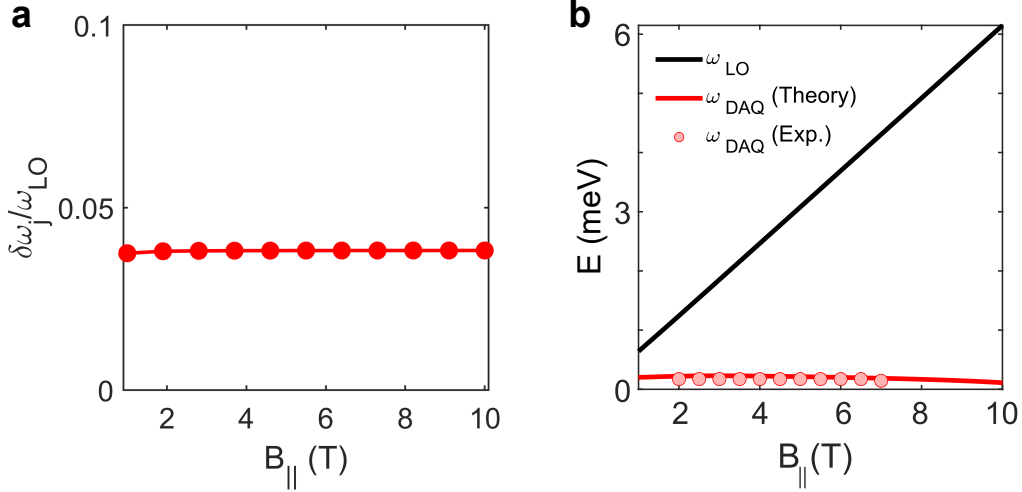


Figure S40: **a**, $\delta\omega_j/\omega_{\text{LO}}$ as a function of B_{\parallel} . **b**, ω_{LO} , which is given by $\sqrt{\omega_{\text{DAQ}}^2 + C^2 B_{\parallel}^2}$, is shown as a function of B_{\parallel} .

III.2 Future steps to build a functioning Axion detector

We describe the future experimental preparations that are needed in order to build a functional Axion detector based on our DAQ material.

1. Sample size: For the photon counting approach, we need the sample area needs to be 0.16 m^2 and the thickness of 0.4 mm. MnBi_2Te_4 has been grown by MBE [14] which solves the sample area issue. Large thickness is more challenging. As shown in the main text, the DAQ in 6L MnBi_2Te_4 relies on the finite thickness hybridization gap. We propose to grow mm-thick samples that consist of repeating superlattice between 6L MnBi_2Te_4 and spacer layer such as Al_2O_3 . In this way, the 6L MnBi_2Te_4 films are isolated from each other but the total thickness can be large. We can first test the superlattice with smaller total thickness (e.g. 100nm) to optimize its quality and growth speed. Then we can grow a 0.4 mm thickness superlattice, which we estimate to take multiple weeks [15]. Apart from MnBi_2Te_4 , $\text{Mn}_2\text{Bi}_2\text{Te}_5$ is a new bulk crystal that can be viewed as a natural superlattice between bilayer MnBi_2Te_4 and Bi_2Te_3 , where theory has predicted large DAQ [16]. Large, mm size single crystals have been synthesized [17,18]. Beyond the Mn-Bi-Te based materials, we have discussed the possibility of searching for large DAQ in multiferroic insulators, which can be a future direction.

2. Directly measure Axion polariton: In our current experiments, we used a pump laser of visible photons ($\hbar\omega \simeq 2.5 \text{ eV}$), which is off resonance and relies on the laser-heating induced coherent spin wave excitation. Hence our pump laser only excited the DAQ (i.e., the out-of-plane magnon) at frequency/mass $m_{\text{DM}} = 44 \text{ GHz} = 0.18 \text{ meV}$. If we use low energy photons that are close to the resonance, then those photons and the DAQ (i.e., the out-of-plane magnon) can hybridize to form Axion polaritons (magnon polaritons), which can be understood as the gap opening and level-repel picture shown in Fig. S41. The top of the gap is at energy $\sqrt{m_{\text{DAQ}}^2 + C^2 B_{\parallel}^2}$, which grows with magnetic field B_{\parallel} . Such an Axion polariton can be directly measured on our 6L MnBi_2Te_4 by the scanning near-field optical microscope (SNORM) [19].

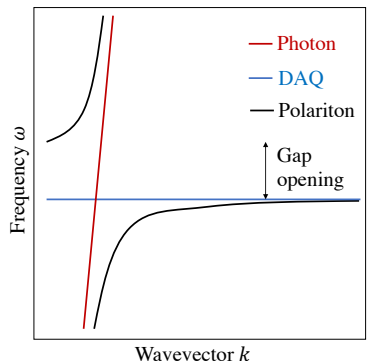


Figure S41: Polariton.

3. Losses: Material imperfection (residue conductivity and magnetic impurities) can lead to damping of the electromagnetic waves inside the material. Right now we have $\Gamma_\rho = 0.2 \times 10^{-3}$ and $\Gamma_m = 0.7 \times 10^{-3}$. If we can improve the sample purity, especially suppressing the residual conductivity and reduce the Mn antisite defects, then one can reach the higher sensitivity than the results in Fig. 4g of main text.

4. Single photon detector efficiency: The single photon detector in the THz regime is rapidly developing. We estimate our sensitivity based on a THz single-photon detector with efficiency $\sim 95\%$ and dark-count rate of 10^{-5} Hz. This is a reasonable projection because the superconducting nanowire single-photon detector has achieved simultaneously such a low dark count and high efficiency in near infrared regime [20, 21]. The same technology is progressing steadily to the longer wavelength [22] where our DAQ detector shall be able to search for the dark matter axions.

III.3 Comparison between the meV DAQ detector and two other proposed future detectors

There is no existing detector in the meV regime. The only two proposed future detectors (called BRASS [23] and BREAD [24]) are based on the same detection mechanism: under a B field, use a giant focusing mirror to focus all dark matter-induced photons (independent of their frequencies) and detect them with single-photon detectors. The earlier BRASS proposal considered a parabolic focusing mirror, which is difficult to integrate into a dilution refrigerator. The more recent BREAD proposal considered a conical focusing mirror that can be compatible with a dilution refrigerator.

We list the pros and cons for our DAQ detector when comparing these two proposed detectors.

Advantages:

- **Frequency resolution and tunability:** At a given magnetic field, the DAQ detector is only sensitive to a particular frequency given by $\sqrt{m_{\text{DAQ}}^2 + C^2 B^2}$. By varying the magnetic field, we can scan different frequencies. By contrast, the BRASS and BREAD focus all photons independent of their frequencies and detect them at once (if using the single photon detectors with better signal to noise). Therefore, their approach loses all information on the photon frequency, and thus on the axion mass, whereas the DAQ approach would immediately give the axion mass.
- **Economy:** The BRASS and BREAD essentially collect all photons without resonant enhancement. Therefore, to get a large signal requires a large focusing mirror. To achieve sufficient sensitivity, the area of the mirror was estimated to be $A = 10 \text{ m}^2$. For BRASS, the parabolic mirror is incompatible with dil fridge. For BREAD, a $A = 10 \text{ m}^2$ solenoidal focusing mirror requires a very large dil fridge with magnet to house it. This is estimated to cost about tens of millions USD. By contrast, the DAQ sample can easily fit in any commercially available dil fridge, which costs about 600K USD.

Disadvantages:

- **Scanning time and sensitivity:** The key disadvantage of the DAQ approach is the need to scan many frequencies. In our estimations in the main text, the measurement time on a single frequency is $\delta\tau = 50$ minutes, while the total measurement time is $\tau = 3$ years. By contrast, the BRASS and BREAD can detect a wide range of frequencies at the same time simultaneously, but with no frequency resolution and no boost factor. Our estimation found that the broadband approach is more sensitive than our proposed DAQ detector by a factor of around 5 (see detailed calculation below). Improving the loss factor of the DAQ material in future (increase β), and using larger/multiple samples to increase the area then the DAQ sensitivity can be comparable with the broadband approach.

For the broadband approach, to cover a wide range requires multiple receivers. BRASS estimated $N = 9$ receivers in their proposed range [25]. For the same photon detector, the sensitivity in the broadband approach compared to the DAQ approach is:

$$\frac{g^{\text{res.}}}{g^{\text{b.b.}}} = \frac{1}{\beta} \sqrt{\frac{A^{\text{b.b.}} \tau}{A^{\text{res.}} \delta\tau}}. \quad (\text{S3})$$

For $\beta \approx 100$, $\delta\tau = 50$ min and $\tau = 3$ years/ N and equal areas the approaches are comparably sensitive, with β compensating the differing measurement time. Using our area of $A^{\text{res}} = 0.16 \text{ m}^2$ compared to BREAD [24] $A^{\text{b.b.}} = 10 \text{ m}^2$ the broadband approach is more sensitive than our proposed DAQ detector by a factor of around 5. Note that this improved sensitivity is only achieved once the total campaign has been completed. The resonant DAQ detector achieves design sensitivity on each frequency in a shorter time.

IV. Theoretical derivation for the layer Hall effect

As a \mathcal{PT} -symmetric material, even-layer MnBi_2Te_4 hosts the so-called layer Hall effect [26], which manifests as an out-of-plane E_z -induced AHE. Here we show that the electric-field-induced AHE σ_{xy} measures $d\mathcal{D}/dn$. The anomalous Hall conductivity is given by

$$\sigma_{xy} = \frac{e^2}{2\pi h} \int_{\varepsilon_{n\mathbf{k}} \leq \mu} \Omega(\mathbf{k}) d\mathbf{k} \quad (\text{S4})$$

$$= \frac{e^2}{2\pi h} \int_{\varepsilon_{n\mathbf{k}} \leq \mu} [\Omega_T(\mathbf{k}) + \Omega_B(\mathbf{k})] d\mathbf{k} \quad (\text{S5})$$

In the second line, we have used the fact that in MnBi_2Te_4 , the Berry curvature is dominated by the low-energy surface bands localized on the top and bottom surfaces. Because we have $\Omega_T = -\Omega_B$, the AHE conductivity vanishes in even-layer MnBi_2Te_4 . Upon applying the out-of-plane electric field E_z , E_z creates an imbalance of chemical potential (charge density, Δn) between the top and bottom layers. Therefore, the AHE conductivity under finite E_z is given by

$$\begin{aligned} \sigma_{xy} &= \frac{e^2}{2\pi h} \int_{\varepsilon_{n\mathbf{k}} \leq \mu} [\Omega_T(\mathbf{k}, n + \Delta n) + \Omega_B(\mathbf{k}, n - \Delta n)] d\mathbf{k} \\ &= \frac{e^2}{2\pi h} \int_{\varepsilon_{n\mathbf{k}} \leq \mu} \left[\frac{\partial \Omega_T(\mathbf{k}, n)}{\partial n} \Delta n + \frac{\partial \Omega_B(\mathbf{k}, n)}{\partial n} (-\Delta n) \right] d\mathbf{k} \\ &= \frac{1}{2} \frac{\partial \mathcal{D}}{\partial n} (\Delta n) \end{aligned}$$

The charge density imbalance Δn is induced by the out-of-plane electric field E_z , which is further related by the top and bottom gate voltages: $\Delta n = \frac{eE_z}{e} = \frac{\epsilon_0}{2e} \left(\frac{\epsilon_{\text{SiO}_2} V_{\text{BG}}}{h_{\text{SiO}_2}} - \frac{\epsilon_{\text{hBN}} V_{\text{TG}}}{h_{\text{hBN}}} \right)$. Here ϵ_{SiO_2} and ϵ_{hBN} are the dielectric constant of SiO_2 and hBN . h_{SiO_2} and h_{hBN} are the thickness of SiO_2 and hBN . Therefore,

$$\sigma_{xy} = \frac{1}{2} \frac{\partial \mathcal{D}}{\partial n} \left(\frac{\epsilon_0}{2e} \left(\frac{\epsilon_{\text{SiO}_2} V_{\text{BG}}}{h_{\text{SiO}_2}} - \frac{\epsilon_{\text{hBN}} V_{\text{TG}}}{h_{\text{hBN}}} \right) \right)$$

In other words, by measuring the E_z -induced σ_{xy} using transport and knowing the value of the applied gate voltages V_{TG} and V_{BG} , we can obtain $\frac{\partial \mathcal{D}}{\partial n}$ as shown in Extended Data Fig.4.

V. Tight binding model for MnBi₂Te₄

The tight binding model Hamiltonian used in order to describe the few layer MnBi₂Te₄ was inspired by the earlier works on Bi₂Te₃, where the low energy bands are represented by the bonding ($P1_z^+$) and the anti-bonding ($P2_z^-$) states formed by Bi p_z and Te p_z orbitals [27]. The model is designed to describe four low energy bands (including the spin degrees of freedom) per quintuple layer near the $\Gamma(0,0,0)$, point. The basis set is given by,

$$|P1_z^+, \uparrow\rangle, |P2_z^-, \uparrow\rangle, |P1_z^+, \downarrow\rangle, |P2_z^-, \downarrow\rangle. \quad (\text{S6})$$

The \pm sign denote the parity of the states, while the \uparrow, \downarrow indicate the spins in the z direction. Various symmetry aspects of this model is explained in detail in Ref [28] as well as in Ref [29]. The bulk Hamiltonian without any magnetization is expressed as,

$$\begin{aligned} h_{TB} = & [e_0 - 2t_0(\cos k_1 a + \cos k_2 a + \cos k_3 a) - 2t_0^z \cos k_4 a_z] \Gamma_0 \\ & - t_1(2 \sin k_1 a - \sin k_2 a - \sin k_3 a) \Gamma_1 - \sqrt{3} t_1 (\sin k_2 a - \sin k_3 a) \Gamma_2 \\ & - 2t_3^z \sin k_4 a_z \Gamma_3 - 2t_4 (\sin k_1 a + \sin k_2 a + \sin k_3 a) \Gamma_4 \\ & + [e_5 - 2t_5(\cos k_1 a + \cos k_2 a + \cos k_3 a) - 2t_5^z \cos k_4 a_z] \Gamma_5 \end{aligned} \quad (\text{S7})$$

The Γ matrices are given by, $\Gamma_0 = I_4$, $\Gamma_1 = s_x \tau_x$, $\Gamma_2 = s_y \tau_x$, $\Gamma_3 = s_z \tau_x$, $\Gamma_4 = s_0 \tau_y$, $\Gamma_5 = s_0 \tau_z$. Here the s and τ represents the spin and the orbital degrees of freedom, respectively. The crystal momentum, $k_1 = k_x$, $k_2 = \frac{1}{2}(-k_x + \sqrt{3}k_y)$, $k_3 = \frac{1}{2}(-k_x - \sqrt{3}k_y)$, $k_4 = k_z$.

Here,

$$\begin{aligned} e_0 &= C_0 + 2C_1/a_z^2 + 4C_2/a^2, \\ e_5 &= M_0 + 2M_1/a_z^2 + 4M_2/a^2, \\ t_0 &= \frac{2C_2}{3a^2}, \\ t_0^z &= \frac{C_1}{a_z^2}, \\ t_1 &= -\frac{A_2}{3a}, \\ t_3^z &= -\frac{A_1}{2a_z}, \\ t_5 &= \frac{2M_2}{3a^2}, \\ t_5^z &= \frac{M_1}{a_z^2}. \end{aligned} \quad (\text{S8})$$

The parameters used are listed below:

$$\begin{aligned} C_0 &= -0.0048 \text{ eV}, \\ C_1 &= 2.7232 \text{ eV}\text{\AA}^2, \\ C_2 &= 0 \text{ eV}\text{\AA}^2, \\ M_0 &= -0.1165 \text{ eV}, \\ M_1 &= 11.9048 \text{ eV}\text{\AA}^2, \\ M_2 &= 9.4048 \text{ eV}\text{\AA}^2, \\ A_1 &= 4.0535 \text{ eV}\text{\AA}, \\ A_2 &= 3.1964 \text{ eV}\text{\AA}, \\ a &= 4.334 \text{ \AA}, \\ a_z &= \frac{1}{3}c = \frac{40.91}{3} = 13.64 \text{ \AA}. \end{aligned} \quad (\text{S9})$$

The few-layer thick MnBi_2Te_4 is modeled by discretizing the bulk Hamiltonian along the z direction and coupling individual MnBi_2Te_4 layers with symmetry allowed interlayer hoppings. The AFM order is included by adding a layer-dependent exchange coupling to the non-magnetic Hamiltonian [30]. In the layer basis, the magnetic part of the Hamiltonian is expressed as,

$$h_{AFM} = \begin{bmatrix} \mathbf{m_A} \cdot \mathbf{s} \otimes \tau_0 & 0 \\ 0 & \mathbf{m_B} \cdot \mathbf{s} \otimes \tau_0 \end{bmatrix} \quad (\text{S10})$$

Here, A and B represent the two layers of the AFM unit cell. Different spin configurations representative of the magnon modes are described by controlling the magnetization parameter of each layer, $\mathbf{m}_i = m_i \hat{m}_i$, where, the $\hat{m}_i = (\cos \phi_i \sin \theta_i, \sin \phi_i \sin \theta_i, \cos \theta_i)$ is the unit vector along the direction of the magnetic moment. The θ and ϕ represent the angles of the spherical polar coordinates. In order to model the pristine MnBi_2Te_4 thinfilm with the out-of-plane AFM order, we have used $m_A = m_B = 30$ meV, and $\theta_A = \pi$, $\theta_B = 0$, $\phi_A = \phi_B = 0$.

VI. Additional discussion

1. The polar Kerr rotation can arise from the normal Kerr proportional to M_z as well as the AFM Kerr proportional to L_z . By the symmetry analysis, one can show that the AFM Kerr can NOT have any linear-to- E contribution, so the linear-to- E Kerr rotation can only arise from the normal Kerr proportional to M_z . The symmetry analysis is as follows: The AFM Kerr has distinct symmetry properties; it breaks P and T but respects PT . As a result, suppose the AFM Kerr has a linear- E component: AFM Kerr = χE . We can perform PT operation to both sides of the equation. Under PT , AFM Kerr is invariant, but E becomes $-E$. Therefore $\chi = 0$. In other words, the AFM Kerr effect cannot have any linear- E component (it can only have even powers of E including E^0). Therefore, the linear- E dependent Kerr purely comes from the E -induced magnetization, i.e., the magnetoelectric coupling.
2. Our experiments focused on a relatively small doping range $\pm 8 \times 10^{12} \text{ cm}^{-2}$ near charge neutrality; Within this small range near charge neutrality, our data demonstrate that the magnetic properties of MnBi₂Te₄ are roughly unchanged. On the other hand, if one accesses much larger doping level, it is entirely possible that J and K of MnBi₂Te₄ could be modified due to the $p-d$ coupling. Here, we provide some rough estimation according to previous works. In Ref. [31], the authors studied the T_c of Mn-doped Bi₂(Te/Se)₃ as a function of n . It was shown (Fig. 2 of that paper) that T_c starts to change as n goes beyond 10^{13} cm^{-2} . It should be noted that in Mn-doped Bi₂(Te/Se)₃, Mn ions are dilute and randomly distributed, so the Mn-Mn exchange coupling entirely relies on the RKKY interaction ($p-d$ coupling) through the itinerant electrons. By contrast, in MnBi₂Te₄, the exchange coupling mainly arises from the Mn-Mn super-exchange. Therefore, it is reasonable to expect that, in order to for MnBi₂Te₄ to show a strong change of T_N (therefore magnetism), one would need to vary n to an even larger value such as high 10^{13} or 10^{13} cm^{-2} .
3. Why the magnetoelectric (ME) coupling α is zero above T_N , even though MnBi₂Te₄ in the nonmagnetic state is topologically nontrivial:

First, as a starting point, this ($\alpha = 0$) can be argued by a general symmetry analysis. The magnetoelectric (ME) coupling can be expressed by $M = \alpha E$. We apply time-reversal operation to both sides of the equation, under which M flips sign but E remains invariant. Therefore, the only way for this to make sense is to have $\alpha = 0$, i.e., the ME coupling α vanishes with time-reversal symmetry. This symmetry requirement is general, meaning that it is true for any kind of ME coupling (topological or trivial).

Second, we discuss specifically for the case of strong TI with time-reversal symmetry. The strong TI has a nontrivial θ , but it only manifests as a quantized α if we gap out the Dirac surface states. This can be seen from the pioneering theory papers. For example, in the following two theoretical works [32,33], the authors showed the proposed setup to observe quantized α (see Fig. 15a of Ref. [32] and Fig. 2b of Ref. [33]). In both works, the strong TI is interfaced with ferromagnetic insulators so that the Dirac surface states are gapped. In this setup, the bulk (i.e., the interior) of the TI can still remain time-reversal symmetric, but the surface is gapped out by interfacial time-reversal breaking. The gapped Dirac surface states have a nonzero Hall conductivity, and the Hall current wraps around the sample, generating the quantized α . By contrast, if we have a stand-alone strong TI without the ferromagnetic insulators, then the strong TI has gapless Dirac surface states. The entire sample, which includes the bulk and the surfaces, have time-reversal symmetry. Then the α should vanish because of the time-reversal symmetry of the entire sample, even though the system has nontrivial topology. This fact has also been explicitly stated by another early theory paper [34]: Quote: “Next we analyze the case of a strong \mathcal{Z}_2 topological insulator having $\theta = \pi$, or equivalently. We first consider a sample of such a system that has T symmetry conserved at its surfaces, as in Fig. 1(a). Again, since the entire sample is T -symmetric, its experimentally measurable magnetoelectric coupling tensor β clearly has to vanish”. (Their β is our α here).

References

- [1] Bartram, F. M. *et al.* Real-time observation of magnetization and magnon dynamics in a two-dimensional topological antiferromagnet MnBi₂Te₄. *Sci. Bull.* **68**, 2734–2742 (2023).
- [2] Van Kampen, M. *et al.* All-optical probe of coherent spin waves. *Phys. Rev. Lett.* **88**, 227201 (2002).
- [3] Qiu, J.-X. *et al.* Axion optical induction of antiferromagnetic order. *Nat. Mater.* **22**, 583–590 (2023).
- [4] Bartram, F. M. *et al.* Ultrafast coherent interlayer phonon dynamics in atomically thin layers of MnBi₂Te₄. *npj Quantum Mater.* **7**, 84 (2022).
- [5] Krichevskov, B. B., Pavlov, V. V., Pisarev, R. V. & Gridnev, V. N. Spontaneous non-reciprocal reflection of light from antiferromagnetic Cr₂O₃. *J. Phys. Condens. Matter* **5**, 8233 (1993).
- [6] Hendriks, F., Rojas-Lopez, R. R., Koopmans, B. & Guimarães, M. H. Electric control of optically-induced magnetization dynamics in a van der waals ferromagnetic semiconductor. *Nature Commun.* **15**, 1298 (2024).
- [7] Zhang, X.-X. *et al.* Gate-tunable spin waves in antiferromagnetic atomic bilayers. *Nature Mater.* **19**, 838–842 (2020).
- [8] Schütte-Engel, J. *et al.* Axion quasiparticles for axion dark matter detection. *J. Cosmol. Astropart. Phys.* **2021**, 066 (2021).
- [9] Tanabashi, M. *et al.* Review of particle physics. *Phys. Rev. D* **98** (2018).
- [10] Bayrakci, S. *et al.* Lifetimes of antiferromagnetic magnons in two and three dimensions: Experiment, theory, and numerics. *Phys. Rev. Lett.* **111**, 017204 (2013).
- [11] Zhao, Y.-F. *et al.* Even–odd layer-dependent anomalous hall effect in topological magnet MnBi₂Te₄ thin films. *Nano Lett.* **21**, 7691–7698 (2021).
- [12] Lee, G.-H. *et al.* Graphene-based josephson junction microwave bolometer. *Nature* **586**, 42–46 (2020).
- [13] Li, R., Wang, J., Qi, X.-L. & Zhang, S.-C. Dynamical axion field in topological magnetic insulators. *Nature Phys.* **6**, 284–288 (2010).
- [14] Bai, Y. *et al.* Chern insulator phase realized in dual-gate-tuned MnBi₂Te₄ thin films grown by molecular beam epitaxy. *arXiv preprint arXiv:2406.05676* (2024).
- [15] Novikov, S. V., Staddon, C. R., Whale, J., Kent, A. J. & Foxon, C. T. Growth of free-standing wurtzite algan by mbe using a highly efficient rf plasma source. *Journal of Vacuum Science & Technology B* **34** (2016).
- [16] Zhang, J. *et al.* Large dynamical axion field in topological antiferromagnetic insulator Mn₂Bi₂Te₅. *Chin. Phys. Lett.* **37**, 077304 (2020).
- [17] Cao, L. *et al.* Growth and characterization of the dynamical axion insulator candidate Mn₂Bi₂Te₅ with intrinsic antiferromagnetism. *Phy. Rev. B* **104**, 054421 (2021).
- [18] Qian, T. *et al.* Single crystal growth, chemical defects, magnetic and transport properties of antiferromagnetic topological insulators (Ge_{1-δ-x}Mn_x)₂Bi₂Te₅ ($x \leq 0.47$, $0.11 \leq \delta \leq 0.12$). *arXiv preprint arXiv:2404.17764* (2024).
- [19] Basov, D., Fogler, M. & de Abajo, F. G. Polaritons in van der Waals materials. *Science* **354**, aag1992 (2016).
- [20] Marsili, F. *et al.* Detecting single infrared photons with 93% system efficiency. *Nature Photon.* **7**, 210–214 (2013).
- [21] Gambetta, J. M. *et al.* Investigating surface loss effects in superconducting transmon qubits. *IEEE Trans. Appl. Supercond.* **27**, 1–5 (2016).

- [22] Verma, V. *et al.* Single-photon detection in the mid-infrared up to $10 \mu\text{m}$ wavelength using tungsten silicide superconducting nanowire detectors. *APL photonic* **6** (2021).
- [23] Horns, D. *et al.* Searching for WISPy cold dark matter with a dish antenna. *J. Cosmol. and Astropart. Phys.* **2013**, 016 (2013).
- [24] Liu, J. *et al.* Broadband solenoidal haloscope for terahertz axion detection. *Phys. Rev. Lett.* **128**, 131801 (2022).
- [25] Bajjali, F. *et al.* First results from BRASS-p broadband searches for hidden photon dark matter. *JCAP* **08**, 077 (2023). 2306.05934.
- [26] Gao, A. *et al.* Layer Hall effect in a 2D topological axion antiferromagnet. *Nature* **595**, 521–525 (2021).
- [27] Zhang, H. *et al.* Topological insulators in Bi_2Se_3 , Bi_2Te_3 and Sb_2Te_3 with a single dirac cone on the surface. *Nature Phys.* **5**, 438–442 (2009).
- [28] Ahn, J., Xu, S.-Y. & Vishwanath, A. Theory of optical axion electrodynamics and application to the Kerr effect in topological antiferromagnets. *Nature Commun.* **13**, 7615 (2022).
- [29] Zhang, D. *et al.* Topological axion states in the magnetic insulator MnBi_2Te_4 with the quantized magnetoelectric effect. *Phys. Rev. Lett.* **122**, 206401 (2019).
- [30] Zhang, R.-X., Wu, F. & Das Sarma, S. Möbius insulator and higher-order topology in $\text{MnBi}_{2n}\text{Te}_{3n+1}$. *Phys. Rev. Lett.* **124**, 136407 (2020).
- [31] Checkelsky, J. G., Ye, J., Onose, Y., Iwasa, Y. & Tokura, Y. Dirac-fermion-mediated ferromagnetism in a topological insulator. *Nature Phys.* **8**, 729–733 (2012).
- [32] Qi, X.-L., Hughes, T. L. & Zhang, S.-C. Topological field theory of time-reversal invariant insulators. *Phys. Rev. B* **78**, 195424 (2008).
- [33] Wang, J., Lian, B., Qi, X.-L. & Zhang, S.-C. Quantized topological magnetoelectric effect of the zero-plateau quantum anomalous Hall state. *Phys. Rev. B* **92**, 081107 (2015).
- [34] Coh, S., Vanderbilt, D., Malashevich, A. & Souza, I. Chern-simons orbital magnetoelectric coupling in generic insulators. *Phys. Rev. B* **83**, 085108 (2011).